Progressive overfilling of readily releasable pool underlies short-term facilitation at recurrent excitatory synapses in layer 2/3 of the rat prefrontal cortex

Jiwoo Shin[1,2], Seung Yeon Lee[2], Yujin Kim[1,2*], Suk-Ho Lee[1,2*]

1. Department of Brain and Cognitive Sciences, College of Natural Sciences, Seoul National University. 2. Department of Physiology, Seoul National University College of Medicine. 03080, Seoul, South Korea.

* *corresponding authors*

Yujin Kim Ph.D. (kim.y@snu.ac.kr)
Cell Physiology Lab
Department of Physiology
Seoul National Univ. College of Medicine

Suk-Ho Lee M.D., Ph.D. (leesukho@snu.ac.kr)
Cell Physiology Lab
Department of Physiology
Seoul National Univ. College of Medicine
103 Daehakro, 03080, Seoul, South Korea
Phone) +82-2-740-8222

Abstract

Short-term facilitation of recurrent excitatory synapses within the cortical network has been proposed to support persistent activity during working memory tasks, yet the underlying mechanisms remain poorly understood. We characterized short-term plasticity at the local excitatory synapses in layer 2/3 of the rat medial prefrontal cortex and studied its presynaptic mechanisms. Low-frequency stimulation induced slowly developing facilitation, whereas high-frequency stimulation initially induced strong depression followed by rapid facilitation. This non-monotonic delayed facilitation after a brief depression resulted from a high vesicular fusion probability and slow activation of Ca^{2+}-dependent vesicle replenishment, which led to the overfilling of release sites beyond their basal occupancy. Pharmacological and gene knockdown (KD) experiments revealed that the facilitation was mediated by phospholipase C/diacylglycerol signaling and synaptotagmin 7 (Syt7). Notably, Syt7 KD abolished facilitation and slowed the refilling rate of vesicles with high fusion probability. Furthermore, Syt7 deficiency in layer 2/3 pyramidal neurons impaired the acquisition of trace fear memory and reduced c-Fos activity. In conclusion, Ca^{2+}- and Syt7-dependent overfilling of release sites mediates synaptic facilitation at layer 2/3 recurrent excitatory synapses and contributes to temporal associative learning.

Introduction

Synapses in the mammalian central nervous system undergo activity-dependent modulation of synaptic weight during repetitive stimulation, known as short-term synaptic plasticity (STP). STP is mediated by presynaptic mechanisms that regulate the release probability (p_r), size of the readily releasable pool (RRP), and kinetics of vesicle replenishment of RRP (Zucker and Regehr, 2002; Jackman and Regehr, 2017; Neher and Brose, 2018). Short-term depression has been observed at synapses with a high baseline p_r, primarily because of the rapid depletion of releasable vesicles during high-frequency stimulation (HFS) (Lin et al., 2022). Conversely, vesicle depletion is less pronounced at synapses with a low baseline p_r, and cumulative increases in p_r during HFS are considered to mediate short-term facilitation (Rozov et al., 2001; Pan and Zucker, 2009; Aldahabi et al., 2024). Central synapses exhibit a wide spectrum of STP depending on different combinations of presynaptic factors mediating short-term depression and facilitation.

Previously, facilitation was modeled as an increase in p_r after an action potential (AP) and its slow decay during the inter-spike interval (ISI), resulting in a cumulative increase in p_r during HFS (Markram et al., 1998; Dittman et al., 2000). Recent studies have suggested that the number of docking (or release) sites in an active zone is limited and only partially occupied by releasable vesicles in the resting states (Miki et al., 2016; Pulido and Marty, 2018; Malagon et al., 2020; Lin et al., 2022). Therefore, p_r is determined by the vesicular fusion probability (p_v) and release site occupancy (p_{occ}). However, distinguishing the individual contributions of p_v and p_{occ} to p_r is challenging (Silva et al., 2021; Neher, 2024). It is also unclear whether facilitation is mediated by activity-dependent increases in the p_v, p_{occ}, or both.

63 Two recent models for vesicle priming and release view the 'priming' as a two-step reversible
64 process that leads to a release-ready state. The release-ready vesicles could be vesicles in a
65 tightly docked state (TS) or those occupying specialized docking sites (DS), and are supplied
66 from vesicles in a loosely docked state (LS) or those occupying a distinct replacement sites
67 (RS), which are called LS/TS model (Aldahabi et al., 2024; Neher, 2024) and RS/DS model (Miki
68 et al., 2016; Silva et al., 2021), respectively. Common to both models is the assumption that
69 release-ready vesicles constitute only a fraction of all docked vesicles under resting conditions
70 and that this fraction is up- and down-regulated by synaptic activity.
71 Synaptotagmin-7 (Syt7) was recently found to play a crucial role in facilitation at different
72 types of central synapses (Jackman et al., 2016; Chen et al., 2017; Martinetti et al., 2022). In
73 addition to its role in facilitation, Syt7 accelerates refilling of the RRP after depletion and
74 mediates asynchronous release (Bacaj et al., 2013; Liu et al., 2014; Jackman et al., 2016;
75 Tawfik et al., 2021). Syt7-dependent synaptic facilitation is interpreted as an activity-
76 dependent increase in p_v (Turecek et al., 2016; Jackman and Regehr, 2017; Turecek et al., 2017;
77 Norman et al., 2023). However, it is unclear whether Syt7 contributes to facilitation through
78 a Ca^{2+}-dependent increase in p_{occ} (i.e., overfilling). Overfilling has been proposed as a
79 mechanism supporting facilitation at the Drosophila neuromuscular junction (Kobbersmed et
80 al., 2020), yet whether this process also occurs at the mammalian central synapses mediated
81 by Syt7 has not been studied.
82 Each of layer 2/3 (L2/3) and layer 5 (L5) of neocortex displays intralaminar excitatory synapses
83 between pyramidal cells comprising a recurrent network (Holmgren et al., 2003; Thomson
84 and Lamy, 2007). Short-term facilitation at recurrent excitatory synapses in a cortical network

may play a crucial role in maintaining working memory (Mongillo et al., 2008; Mongillo et al., 2012; Hansel and Mato, 2013). Although L2/3 pyramidal cells (PCs) represent task-relevant information during a delay period in working memory tasks (Fujisawa et al., 2008; Ozdemir et al., 2020), most studies on local excitatory recurrent synapses in the neocortex have focused on L5 exhibiting short-term depression (Reyes and Sakmann, 1999; Hempel et al., 2000; Yoon et al., 2020). Further, the synaptic properties of excitatory synapses in L2/3 remain poorly understood.

In the present study, we found that HFS of local excitatory synapses in L2/3 of the medial prefrontal cortex (mPFC) induced initial strong depression followed by delayed facilitation, whereas low-frequency stimulation induced slow monotonous facilitation. This unique form of STP could be explained by 1) high p_v of RRP vesicles at rest and throughout a train stimulation; 2) the low resting vesicular occupancy of RRP and its activity-dependent increase. These conditions led to delayed facilitation through progressive overfilling of release sites during HFS with high p_v vesicles beyond the resting occupancy. Syt7 knockdown (KD) in L2/3 PCs completely abolished these synaptic enhancements by inhibiting the Ca^{2+}-dependent increase in release site occupancy. Finally, behavioral tests for trace fear conditioning showed that Syt7 KD impaired the acquisition of trace fear memory and reduced c-Fos expression in the mPFC. Collectively, these results support that Ca^{2+}- and Syt7-dependent overfilling of release sites mediates synaptic facilitation at L2/3 recurrent excitatory synapses and contributes to temporal associative learning.

106 ## Results

107 *Frequency dependence of STP at local excitatory synapses in L2/3 of the prelimbic cortex*

108 We examined STP profiles at recurrent excitatory synapses between L2/3 PCs and at synapses
109 from L2/3-PCs to fast-spiking interneurons (FSINs) in the prelimbic area of the rat mPFC. The
110 PCs and FSINs were identified based on their distinct intrinsic properties and morphologies
111 (***Figure 1—figure supplement 1***). To stimulate presynaptic PCs, L2/3 PCs were transfected
112 with a plasmid encoding oChIEF using *in utero* electroporation (IUE; ***Figure 1A***; Lee et al.,
113 2024). Photo-stimulation of the oChIEF-expressing cell soma at 40 Hz consistently evoked
114 single APs with high fidelity throughout the 600-pulse trains (***Figure 1—figure supplement***
115 ***2A-B***), which was consistent with little use-dependent inactivation of oChIEF (Lin et al., 2009;
116 Hass and Glickfeld, 2016).
117 Given that IUE transfected approximately 10-20% of L2/3 PCs (***Figure 1A***), we made a whole-
118 cell patch on a non-transfected L2/3 PC or an FSIN (***Figure 1C***). To stimulate a minimal number
119 of excitatory axon fibers, EPSCs were evoked using minimal optical stimulation (***Figure 1—***
120 ***figure supplement 3A***; 470 nm, 3-4 µm in radius and 3-5 ms in duration). EPSCs evoked by
121 minimal stimulation were examined to determine the uniformity of the kinetic properties
122 (***Figure 1—figure supplement 3B-C***). Moreover, we reassessed the kinetics of EPSCs during
123 trains *post hoc* to ensure uniformity. EPSCs were evoked by 20-pulse trains at 4 different
124 frequencies (5, 10, 20, and 40 Hz) to cover the range of firing rates of PCs observed *in vivo*
125 during working memory tasks (Baeg et al., 2003). Excitatory synapses from PCs onto both
126 other PCs and FSINs (PC–PC and PC–FSIN) showed strong (~2-fold enhancement) and lasting

127 (several seconds) short-term facilitation at 20 Hz and lower frequencies (***Figure 1D-E***). The
128 PC-PC synapses exhibited stronger facilitation than did the PC-FSIN synapses.
129 Steady-state EPSCs at the PC-PC synapses were not significantly different from 5 to 20 Hz
130 (***Figure 1F***). Frequency invariance at the PC-PC synapses suggests that Ca^{2+}-dependent
131 synaptic facilitation may counteract vesicle depletion in a frequency-dependent manner
132 (Turecek et al., 2017; Lin et al., 2022). Despite facilitation at all frequencies, the paired pulse
133 ratio (PPR) rapidly decreased as the ISI decreased (***Figure 1G, I***). At 40 Hz stimulation, both
134 PC-PC and PC-FSIN synapses initially underwent strong depression then followed by
135 facilitation in a few stimuli (***Figure 1Dd, Ed***). Such delayed facilitation after paired pulse
136 depression (PPD) has not been previously observed in central synapses except for a slight
137 increase in EPSC at the cerebellar synapses under artificially depolarized conditions (Pulido
138 and Marty, 2018).
139 We confirmed that optically evoked EPSCs were strictly dependent on AP generation (***Figure***
140 ***1—figure supplement 4A***), suggesting that EPSCs are evoked by optical stimulation of
141 presynaptic axon fibers rather than by direct depolarization of presynaptic boutons.
142 Additionally, dual patch-clamp techniques showed that the STP of optically evoked EPSCs did
143 not differ from the electrically evoked STP of EPSCs at the PC-FSIN synapses (***Figure 1—figure***
144 ***supplement 4B***). Finally, we confirmed that AMPA receptor (AMPAR) desensitization was not
145 responsible for PPD at 40 Hz, ruling out the possible effects of postsynaptic factors on STP
146 (***Figure 1—figure supplement 5A***), and that AMPAR saturation was not significant during
147 facilitation (***Figure 1—figure supplement 5B***).
148

149 *Delayed facilitation results from slow activation of Ca^{2+}-dependent vesicle replenishment at a*
150 *constantly high vesicular fusion probability*

151 The strong PPD at 40 Hz suggests a high vesicular fusion probability (p_v) and likely tight
152 coupling of the releasable vesicles to a Ca^{2+} source. To test this hypothesis, we examined the
153 effects of EGTA, a slow calcium chelator, on synaptic transmission at the PC-PC synapses. The
154 baseline EPSC amplitude ($EPSC_1$) was not affected by incubation of the slice in the bath
155 solution containing 50 µM EGTA-AM for longer than 20 min, supporting tight coupling.
156 Moreover, the PPR was decreased to 0.19, and subsequent facilitation slowed but was still
157 distinct (***Figure 2A-B***). These findings indicate that the initial p_v should be higher than 0.81
158 considering vesicle recruitment during ISI. The effects of EGTA-AM were confirmed in the
159 same cell by measuring the baseline EPSC and PPR before and after applying EGTA-AM to the
160 bath. $EPSC_1$ remained unchanged, while PPR was reduced by half (***Figure 2—figure***
161 ***supplement 1***).
162 Notably, the application of EGTA-AM markedly slowed facilitation at 40 Hz (***Figure 2A, C***). The
163 frequency invariance of steady-state EPSCs (***Figure 1F***) and the slower facilitation at 40 Hz in
164 the presence of EGTA (***Figure 2A***) imply a Ca^{2+}-dependent increase in the refilling rate of the
165 RRP and/or an increase in the p_v of reluctant vesicles in light of previous studies (Hosoi et al.,
166 2007; Liu et al., 2014; Ritzau-Jost et al., 2014; Turecek et al., 2016; Ritzau-Jost et al., 2018;
167 Kusick et al., 2020). Moreover, facilitation was accelerated at higher stimulation frequencies.
168 The plot of the rate constant for the increase in EPSCs (denoted as $\mathbf{k}_{STF}$, the rate constant for
169 the development of short-term facilitation) as a function of the stimulation frequency (f_{stim})

170 revealed a linear relationship (***Figure 2C***). $\mathbf{k}_{STF}$ in the presence of EGTA-AM was distinctly
171 below this relationship, supporting the Ca^{2+}-dependent acceleration of facilitation.
172 $\mathbf{k}_{STF}$ was also accelerated when the stimulation frequency was increased from 5 Hz to 40 Hz
173 (***Figure 2D***; 1.27 ± 0.18/s to 24.27 ± 3.44/s). Notably, the second 40-Hz train stimulation led
174 to strong PPD, followed by accelerated facilitation (***Figure 2D-E***). The strong PPD suggests that
175 the vesicular fusion probability kept high during the 5-Hz stimulation, arguing against the
176 possibility for an increase in p_v. Both two-step sequential priming models, LS/TS and RS/DS
177 models, are suitable to interpret our data and we will refer to the different populations of
178 vesicles as TS and LS vesicles, respectively (Taschenberger et al., 2016; Neher and Brose, 2018;
179 Lin et al., 2022; Neher, 2024). Within this framework, vesicles are released from TS with high
180 p_v both in the resting state and during facilitation, and the delayed facilitation is seen as a
181 result of Ca^{2+}-dependent progressive increase in the occupancy of TS vesicles on docking sites.
182

183 *Presynaptic calcium measurements at axonal boutons of L2/3 pyramidal cells*

184 To test contribution of Ca^{2+} channel regulation to STP (Dobrunz et al., 1997; Jackman and
185 Regehr, 2017), we estimated total amount of Ca^{2+} increments during 40 Hz AP trains at axonal
186 boutons of L2/3 PCs in the mPFC. To this end, we measured AP-evoked Ca^{2+} transients (AP-
187 CaTs) using two-dye ratiometry techniques, and estimated calcium binding ratio from AP-CaTs
188 (***Figure 2—figure supplement 2A-C***). Measuring the amplitudes and decay time constants of
189 AP-CaTs at different concentrations of Fluo-5F (150, 250 or 500 µM), and plotting them as a
190 function of calcium binding ratio of Fluo-5F (κ_B), we estimated the amplitude of AP-CaTs (A_{Ca}

191 = 1.16 μM), Ca^{2+} decay time constant (τ_c = 43 ms) in the absence exogenous Ca^{2+} buffer, and
192 endogenous static Ca^{2+} binding ratio (κ_S = 96.4 or 77.3 estimated from ***Figure 2—figure***
193 ***supplement 2D-E***, respectively; *See Materials and Methods*). The resting [Ca^{2+}] ([Ca^{2+}]$_{rest}$) was
194 measured as 50 nM (***Figure 2—figure supplement 2F***). Estimating the total Ca^{2+} increments
195 for the first four AP-CaTs in a 40 Hz train according to Equation 2 (*Materials and Methods*),
196 we found no evidence for inactivation or facilitation of calcium influx during a 40 Hz train
197 (***Figure 2—figure supplement 2G-I***), arguing against the possibility that Ca^{2+} channel
198 inactivation and facilitation contribute to strong PPD and delayed facilitation during a 40 Hz
199 train.
200

201 *Release sites have low baseline occupancy and these are increased during facilitation and post-*
202 *tetanic augmentation*

203 Given that p_v was greater than 0.8, the two-fold increase in EPSC during 20 pulse train
204 stimulations could not be explained by an increase in p_v. Recent studies have shown that
205 vesicle release sites (N) are limited in number and are partially occupied at rest (Miki et al.,
206 2016; Pulido and Marty, 2018; Malagon et al., 2020; Lin et al., 2022). Under such a high p_v,
207 two-fold synaptic facilitation should be attributed to an increase in p_{occ}. The vesicle
208 replenishment rate is accelerated during HFS in a Ca^{2+}-dependent manner (***Figure 2A-C***; Hosoi
209 et al., 2007). This may lead to the overfilling of release sites beyond their basal vesicular
210 occupancy, which in turn may increase EPSC under high p_v. To test this hypothesis, we
211 determined the quantal parameters at the L2/3 local excitatory synapses. We first measured

212 the quantal size from asynchronous release events after replacing extracellular Ca^{2+} with Sr^{2+},
213 as previously described (Yoon et al., 2020) (***Figure 3—figure supplement 1A-B***). The mean
214 and coefficient of variance of the quantal sizes were 24 pA and 0.25 at PC-PC synapses,
215 respectively, and were 30 pA and 0.31 at PC-FSIN synapses (***Figure 3—figure supplement 1C***).
216 Next, we performed a variance-mean (V-M) analysis of phasic EPSCs at excitatory synapses
217 during train stimulation at 5 Hz and 40 Hz (Scheuss et al., 2002). Applying multiple-probability
218 fluctuation analysis (MPFA) using intra-site quantal variability of 0.2 (Valera et al., 2012), the
219 V-M plot was best fitted by the number of release sites (N) of 5.3 and the quantal size (q) of
220 25 pA at the PC-PC synapses (***Figure 3A***). The p_r for $EPSC_1$ was calculated as 0.32. We
221 performed the same analysis for the PC-FSIN synapses and found N = 5.3, q = 35 pA, and p_r
222 for $EPSC_1$ = 0.31 (***Figure 3B***). Our estimate for N was smaller but comparable to the estimate
223 (6.9) at excitatory synapses in L2/3 of the mouse barrel cortex (Holler et al., 2021).
224 The p_r estimate was clearly smaller than the possible minimum value for p_v (0.81) estimated
225 from the PPR data (***Figure 2B***). Given that p_r is a product of p_{occ} and p_v (Neher, 2024), a p_r
226 smaller than p_v indicates the partial occupancy of release sites in the resting state. If synaptic
227 facilitation were mediated by the recruitment of new release sites, it would be accompanied
228 by an increase in the variance of augmented EPSCs (Valera et al., 2012; Kobbersmed et al.,
229 2020). However, the augmented EPSCs during facilitation followed the same parabola in the
230 V-M plot (***Figure 3A-B***). Therefore, facilitation appears to be mediated by the progressive
231 overfilling of a finite number of release sites beyond the basal occupancy. In the next section,
232 we show that p_v is close to unity based on a synaptic failure analysis (***Figure 3—figure***
233 ***supplement 2***). Assuming this, the baseline p_r at the first pulse estimated from the fitted

234 parabolic curve can be largely regarded as a baseline p_{occ} (c.a. 30%), and the two-fold increase
235 in EPSCs during facilitation can be attributed to an increase of up to 60% in p_{occ}.
236 We investigated the time course of recovery from facilitation and post-tetanic augmentation
237 (PTA) by applying dual-train stimulations (30 pulses at 40 Hz) separated by different inter-
238 burst intervals (IBIs; ***Figure 3C-D***). The initial EPSCs in the second train were enhanced by more
239 than twofold, and followed by a strong PPD, suggesting that fusion probability stays high in
240 the IBIs and thus synaptic transmission is carried by TS vesicles. The decay time course of PTA
241 was characterized by two phases (initially fast and later slow; ***Figure 3E***), which may reflect a
242 two-phase Ca^{2+} decay or two distinct recovery processes that occur sequentially. The variance
243 of potentiated EPSCs measured at IBIs of 0.1, 0.2, and 0.5 s was not different from that of
244 EPSCs at the peak of facilitation (filled circles, ***Figure 3A-B***). Given that the same RRP mediates
245 both facilitation and augmentation and that post-tetanic EPSCs is carried by TS vesicles similar
246 to the baseline EPSCs, this plot suggests that PTA, similar to short-term facilitation, is
247 mediated by an increase in the TS vesicle occupancy.
248

249 *Failure rate analysis suggests that vesicular fusion probability is close to one*

250 The vesicle dynamics of STP has been explained using a simple refilling model (Hosoi et al.,
251 2007; Neher and Sakaba, 2008). This model assumes that the vesicles are reversibly docked
252 to a limited number of release sites (N) with forward and reverse rate constants (denoted as
253 k_1 and b_1, respectively). Under the framework of the simple refilling model (see *Materials and*
254 *Methods*), the rate constant for the refilling of the RRP after depletion by the first pulse is the

255 sum of the baseline k_1 and b_1. This is estimated as 23/s from the plot of PPR as a function of
256 ISIs (***Figure 3—figure supplement 2A***). From the baseline occupancy of 0.3 and $p_{occ} = k_1 / (k_1$
257 $+ b_1)$, we estimated k_1 to be 6.9/s.
258 When paired APs were applied with an ISI of 20 ms, the failure rate at 1st pulse, $P(F_1)$, was
259 10.6%, and the probability of two consecutive failures, $P(F_1, F_2)$, was 6.2% (***Figure 3—figure***
260 ***supplement 2A***). From the equation $P(F_1) = (1 – p_r)^N$, p_r was calculated as 0.312 when N = 6,
261 comparable to p_r (= 0.32) estimated from the V-M analysis (***Figure 3A***). We calculated $P(F_1, F_2)$
262 under the framework of a simple refilling model, with p_v and k_1 set as free parameters and
263 other parameters set according to the following relationships: $P(F_1) = (1 – p_r)^N$, $p_r = p_v \cdot p_{occ}$,
264 and $p_{occ} = k_1 / (k_1 + b_1)$. The calculated values for $P(F_1, F_2)$ and their difference from the
265 observed value (6.2%) are shown in the plane of k_1 *vs*. p_v in ***Figure 3—figure supplement 2B-***
266 ***C***. Given that k_1 was greater than 5/s, the difference between the calculated and observed
267 values of $P(F_1,F_2)$ was minimal when $p_v = 1$ (***Figure 3—figure supplement 2C***).
268 To find optimal values for k_1 and p_v that best explain observed probabilities shown in ***Figure***
269 ***3—figure supplement 2Ac***, a cost function was implemented as the sum of squared errors
270 between observed and predicted probability values for the four combinations of success and
271 failure of 1st and 2nd EPSCs as described in *Materials and Methods*. The minimum of the cost
272 function (5.63×10^{-5}) was found at $k_1 = 5.21$/s and $p_v = 0.999$, which predicted $P_{11} = 41.5\%$, P_{10}
273 $= 47.9\%$, $P_{01} = 4.93\%$, and $P_{00} = 5.67\%$ (subscript 1 and 0 denote success and failure,
274 respectively).
275
276

277 *Pharmacological manipulations reveal specific molecular identities underlying vesicle loading*
278 *processes*

279 Our results suggest that the baseline occupancy of TS vesicles is low and that the activity-
280 dependent progressive overfilling of docking sites with TS vesicles is responsible for short-
281 term facilitation and augmentation. To elucidate the specific molecular link between synaptic
282 enhancement and Ca^{2+}-dependent overfilling, we examined the effects of several drugs
283 known to affect vesicle dynamics. We first examined the roles of phospholipase C (PLC) and
284 diacylglycerol (DAG) by applying 5 μM U73122, a PLC inhibitor, or 20 μM 1-oleoyl-2-acetyl-sn-
285 glycerol (OAG), a DAG analog. The STP at 40 Hz and PTA at 0.5-s interval were examined before
286 and after applying each drug to the bath. For both drugs, the facilitation and augmentation
287 were reduced (***Figure 4A-B***). U73122 did not affect the basal EPSC amplitude ($EPSC_1$) but
288 resulted in a stronger PPD, slower facilitation, and lower augmentation (***Figure 4A***). These
289 effects of U73122 suggest the involvement of Ca^{2+}-induced PLC activation in progressive
290 overfilling. In contrast, OAG increased $EPSC_1$ while maintaining a pronounced PPD (***Figure 4B***),
291 indicating an increase in the TS vesicle pool size. Meanwhile, OAG slowed $\mathbf{k}_{STF}$ and reduced
292 augmentation, indicating occlusion of activity-dependent synaptic facilitation. Phorbol esters
293 and DAG are thought to accelerate priming through Munc13 activation (Rhee et al., 2002;
294 Taschenberger et al., 2016; Aldahabi et al., 2022); they also shorten the bridges that interlink
295 docked vesicles with the active zone (AZ) membrane (Papantoniou et al., 2023). Collectively,
296 these suggest that PLC- and DAG-mediated signaling play a role in the overfilling of docking
297 sites underlying short-term facilitation and augmentation.

298 Although the acceleration of Ca^{2+}-dependent vesicle refilling supports rapid facilitation at 40
299 Hz, the later part of the delayed facilitation underwent a slight depression, which was more
300 pronounced during the second burst (***Figure 3D and Figure 4***). Sustained synaptic
301 transmission is limited by the spatial availability of docking sites because it is undermined by
302 accumulation of exocytic remainings in the presynaptic AZ during HFS (Neher, 2010; Haucke
303 et al., 2011). To verify this, we examined the effects of dynasore (100 μM), a specific inhibitor
304 of endocytosis (Macia et al., 2006). The treatment with dynasore did not influence $EPSC_1$ or
305 the early phase of facilitation, but it exacerbated depression during the later phase and
306 attenuated PTA (***Figure 4C***). This suggests that late synaptic transmission during the 40-Hz
307 train is limited by site clearance.
308 Given the involvement of actin polymerization in the multiple steps of vesicle docking and
309 recycling, we examined the effects of 20 μM latrunculin B (LatB), an inhibitor of actin
310 polymerization. The effects of LatB were complicated: (1) $EPSC_1$ was decreased, whereas PPR
311 was increased (***Figure 4Da***) and (2) facilitation and augmentation were reduced (***Figure 4Db***).
312 The latter effect may result from defects in vesicle replenishment rates, either through the
313 impaired physical movement of vesicles or disrupted site clearance (Sakaba and Neher, 2003;
314 Lee et al., 2012; Hallermann and Silver, 2013; Miki et al., 2016), as Ca^{2+}-dependent vesicle
315 refilling mediates facilitation and augmentation (***Figure 2 and Figure 3***). Meanwhile, the
316 former effect might be attributed to a shift in equilibrium in the priming states towards a
317 loosely docked state (LS) at rest. It is unknown whether actin affects vesicular fusogenicity in
318 neurons, although it facilitates multiple steps of vesicle fusion by enhancing membrane
319 tension in neuroendocrine cells (Wu and Chan, 2022).

320

321 *Short-term facilitation at both types of local excitatory synapses in L2/3 is abolished by Syt7*
322 *knockdown*

323 We examined whether Syt7 mediates facilitation at the PC-PC and PC-FSIN synapses in L2/3
324 of the mPFC. To this end, oChIEF and shRNA against Syt7 (shSyt7) were co-expressed in L2/3
325 PCs using IUE. Syt7 KD resulted in a complete loss of facilitation at all tested stimulation
326 frequencies (***Figure 5A-B***). Short-term depression and paired-pulse depression were more
327 pronounced as the stimulation frequency increased, and the frequency invariance of steady-
328 state EPSC was abolished, implying little contribution of Ca^{2+}-dependent vesicle recruitment
329 (***Figure 5C-F***). The lack of facilitation could not be attributed to the failure of APs in
330 presynaptic axons, as optical stimulation elicited reliable APs in Syt7 KD PCs during the 40-Hz
331 train (***Figure 1—figure supplement 2C***). Syt7 KD had little effect on the basal properties,
332 including the peak amplitude, rise/decay time, and time-to-peak, of single AP-induced EPSCs
333 (***Figure 1—figure supplement 3D-E***). Moreover, Syt7 KD did not significantly affect the
334 intrinsic properties of neurons (***Figure 5—figure supplement 1***).
335 To examine whether Syt7 KD had any nonautonomous effects on postsynaptic cells, we
336 measured the quantal size (q) from asynchronous events in the presence of Sr^{2+} and found
337 that the mean quantal size remained unaltered at Syt7 KD synapses (***Figure 3—figure***
338 ***supplement 1C***). This indicated that Syt7 did not influence postsynaptic parameters, including
339 the density and kinetic properties of AMPARs. To test the specificity of shSyt7, we examined
340 whether co-expression of the shRNA-resistant form of Syt7 restored synaptic facilitation in
341 both excitatory synapse types. Presynaptic overexpression of shRNA-resistant Syt7 under the

342 CAG promoter rescued the effect of shRNA at both PC-PC and PC-FSIN synapses (***Figure 5—***
343 ***figure supplement 2***). These results underscore the crucial role of presynaptic Syt7 in
344 mediating short-term facilitation at local excitatory synapses in L2/3 of the mPFC.
345
346 *Syt7 KD synapses exhibit complementary changes in the number of release sites and their*
347 *vesicle occupancy*

348 To estimate the quantal parameters in Syt7 KD synapses, we performed V-M analysis of EPSCs
349 evoked by train stimulation (***Figure 6A-B***). Fitting a parabola to the V-M plot revealed higher
350 baseline p_{occ} in Syt7 KD synapses than in wild-type (WT) synapses for both synapse types (KD,
351 0.68 and 0.42; WT, 0.32 and 0.31 for PC-PC and PC-FSIN synapses, respectively). The p_{occ}
352 monotonously decreased during a train stimulation, as expected from short-term depression.
353 Moreover, the number of release sites (N) was markedly lower in Syt7 KD synapses (N = 3.5)
354 than in WT synapses (N = 5.3; ***Figure 3A***). Next, we examined the PTA induced by the same
355 protocol as in ***Figure 3*** (two 40-Hz train stimulations separated by variable IBIs) at Syt7 KD
356 synapses (***Figure 6C***). The 40 Hz train-induced synaptic depression quickly recovered during
357 IBIs, but no PTA was observed at Syt7 KD synapses, indicating its crucial role in augmentation
358 (***Figure 6D-E***).
359
360 *TS vesicle recovery following depletion is accelerated by Syt7*

361 Syt7 is recognized not only for its crucial role in facilitation, but also for mediating Ca^{2+}-
362 dependent replenishment of releasable vesicles (Liu et al., 2014; Tawfik et al., 2021). Given
363 that facilitation at L2/3 excitatory synapses is driven by progressive overfilling (***Figure 2 and***

364 *Figure 3*), the loss of facilitation at Syt7 KD synapses in the present study implies that Syt7
365 plays a key role in the Ca^{2+}-dependent acceleration of refilling and overfilling of the docking
366 sites with TS vesicles. To test this hypothesis, we examined the recovery kinetics of EPSCs
367 after TS vesicles were depleted by 3 pulses at 40 Hz in wild-type (WT) and Syt7 KD synapses
368 (*Figure 7*). Strong PPD was observed not only in the first burst, but also in the second burst.
369 This suggested that EPSCs in the second burst were mediated by TS vesicles, similar to those
370 in the first burst (*Figure 7A, D*). Therefore, $EPSC_1$ in the second burst can be interpreted as a
371 release from TS vesicles recovering during a given IBI. The recovery time course of $EPSC_1$ in
372 the second burst indicated full recovery of TS vesicles within 100 ms in both excitatory
373 synapse types in WT rats (*Figure 7C, F*). However, this recovery was remarkably slower in Syt7
374 KD synapses, requiring 5 s for full recovery, indicating that TS vesicle recovery was greatly
375 accelerated by Syt7. Overall, synaptic facilitation and augmentation at local excitatory
376 synapses in L2/3 can be ascribed to progressive activity-dependent increases in the occupancy
377 of TS vesicles (*Figure 2 and Figure 3*), in which Syt7 plays a key role.
378

379 *Behavioral consequences of Syt7 KD in L2/3 PCs of the mPFC*

380 We previously proposed that the disparity in STP between the PC-PC and PC-IN synapses
381 results in activity-dependent changes in the ratio of synaptic weights at the PC-PC and PC-IN
382 synapses (J_{ee}/J_{ie}). This may in turn have a profound influence on persistent activity in a
383 recurrent network by biasing the E-I balance (Yoon et al., 2020). Syt7 KD not only eliminated
384 facilitation, but also the activity-dependent increase in the J_{ee}/J_{ie} ratio in the L2/3 network

385 (*Figure 8—figure supplement 1*). This suggests the possibility that Syt7 contributes to the
386 persistent activity during working memory tasks in the L2/3 recurrent network. Trace fear
387 conditioning (tFC) requires associative learning between an auditory cue (conditioned
388 stimulus, CS) and temporally separate aversive events (unconditioned stimulus, US). The
389 formation of trace fear memory requires the prelimbic area of the mPFC and hippocampus.
390 mPFC activity during the trace interval is thought to temporarily hold CS information, enabling
391 the network to associate temporally discontinuous events (i.e., temporal associative learning)
392 (Gilmartin et al., 2013). Synaptic facilitation and augmentation are implicated in temporary
393 memory retention in recurrent networks (Mongillo et al., 2008; Mongillo et al., 2012).
394 Given that Syt7 is crucial for synaptic facilitation (*Figure 5*) and augmentation (*Figure 6*) in
395 prelimbic L2/3 recurrent excitatory synapses, we tested whether trace fear memory
396 formation was impaired in rats with depleted Syt7 transcripts, specifically in the L2/3 PCs of
397 the mPFC. Syt7-targeted shRNA (shSyt7) or scrambled shRNA (Scr) constructs were
398 transfected bilaterally into the L2/3 PCs of the mPFC using IUE (*Figure 8A*). Both the Scr-
399 transfected control and shSyt7-transfected rats underwent tFC training (*Figure 8B*).
400 Consistent with Gilmartin et al. (2013), in which prefrontal persistent firing was
401 optogenetically inhibited, WT and KD animals exhibited similar freezing behavior during this
402 acquisition phase. The following day, the rats were subjected to a tone test in which trace
403 fear memory formation was assessed from the freezing response to a tone alone in a distinct
404 context. Compared to the control group, the shSyt7-transfected group exhibited significantly
405 lower levels of freezing behavior in response to auditory cues during the first four trials,
406 suggesting an impairment in trace memory formation (*Figure 8C*).

407 The tone test was repeated the following day to test for extinction memory formation. Syt7
408 KD animals exhibited much less freezing to the CS (+1d) than did WT animals. Considering the
409 Rescorla-Wagner model (Yau and McNally, 2023), our results suggest that the strength of CS-
410 US associative memory was weaker in KD animals than in WT animals; thus, the acquisition
411 of trace fear memory was impaired by Syt7 KD in the L2/3 PCs of the mPFC.
412 Next, we assessed the locomotor activity and anxiety levels of rats using the open field test
413 (OFT) and elevated plus maze test (EPM). Scr controls and Syt7 KD rats showed similar
414 exploratory patterns, displaying comparable total distance moved and time spent in the
415 periphery of the OFT or the open/closed arms of the EPM (***Figure 8—figure supplement 2***).
416 Previous studies have suggested that the acquisition of trace fear memory requires elevated
417 trace activity in prelimbic PCs (Gilmartin et al., 2013). Given that c-Fos, an immediate early
418 gene, is upregulated following patterned activities in neurons, its expression is considered a
419 reliable indicator of recent neuronal activation (Fields et al., 1997; Guzowski et al., 2005). To
420 investigate the effect of Syt7 on neuronal activity *in vivo* during tFC, animals were sacrificed
421 at the time of peak c-Fos protein expression, approximately 90 min after completion of the
422 behavioral task (Arime and Akiyama, 2017).
423 To elucidate the activation patterns of specific neuronal populations, we performed
424 immunohistochemical co-labeling of c-Fos and GAD67 (a GABAergic interneuron marker)
425 upon tFC acquisition. The density of c-Fos(+) cells and the percentage of c-Fos(+) cells among
426 GAD67(+) cells in all prelimbic layers were significantly lower in Syt7 KD rats than in control
427 rats (***Figure 8F-G***). Additionally, analysis of the proportion of active cells among transfected
428 L2/3 PCs (c-Fos+/GFP+) revealed that Syt7 KD L2/3 PCs were significantly more active than

429 Scr-transfected PCs (*Figure 8H*). This unexpected hyperactivity of Syt7 KD PCs may be
430 attributed to the high reciprocal connectivity between PCs and FSINs in the neocortex
431 (Holmgren et al., 2003; Otsuka and Kawaguchi, 2009), as PCs with short-term depression
432 would transmit less input to FSINs, which in turn would exert less feedback inhibition on
433 reciprocally connected PCs. Collectively, these findings show that the slow activation of
434 vesicle refilling supports various forms of facilitation at excitatory synapses in PFC L2/3, which
435 is essential for neuronal activity during temporal associative learning.

436

437 Discussion

438 The present study characterized STP at local excitatory synapses in the L2/3 network of the
439 rat mPFC at physiological extracellular [Ca^{2+}]. These synapses displayed initial strong
440 depression and then delayed facilitation at 40 Hz, while monotonous slowly developing
441 facilitation was observed at lower frequencies. Our study suggests that such delayed
442 facilitation after a brief depression results from a high p_v (*Figure 2 and Figure 3 and Figure*
443 *3—figure supplement 2*), along with Ca^{2+}-dependent delayed acceleration of vesicle refilling
444 and overfilling (*Figure 2 and Figure 3*). The two-fold increase in EPSC during 20 pulse train
445 stimulations under the condition of such a high p_v suggests a Ca^{2+}-dependent increase in the
446 vesicle replenishment rate during a train; this then leads to overfilling of release sites beyond
447 their incomplete basal occupancy (*Figure 3A-B*). The high p_v and strong PPD did not result
448 from artificial bouton stimulation, AMPAR desensitization, or any potential distortion caused
449 by optogenetic methods (*Figure 1—figure supplements 4 and 5*). Additionally, similar to
450 short-term facilitation, PTA could be explained by an increase in the TS vesicle occupancy

451 (***Figure 3C-E***), consistent with previous studies showing post-tetanic increases in the p_{occ}
452 and/or vesicle pool size at various types of synapses (Lee et al., 2010; Vandael et al., 2020;
453 Tran et al., 2023; Silva et al., 2024). These findings suggest that release sites are partially
454 occupied at rest and that a progressive overfilling of release sites with TS vesicles underlies
455 facilitation and augmentation at intracortical L2/3 excitatory synapses.
456

457 *Definition of vesicular release probability in the present and previous studies*

458 Previous studies suggested that an increase in p_v is responsible for post-tetanic augmentation
459 (Stevens and Wesseling, 1999; Garcia-Perez and Wesseling, 2008) by observing invariance of
460 the RRP size after tetanic stimulation. In these studies, the RRP size was estimated by
461 hypertonic sucrose solution or as the sum of EPSCs evoked 20 Hz/60 pulses train (denoted as
462 'RRP_{hyper}'). Because reluctant vesicles (called LS vesicles) can be quickly converted to TS
463 vesicles (16/s) and are released during a train (Lee et al., 2012), it is likely that the RRP size
464 measured by these methods encompasses both LS and TS vesicles. In contrast, we assert high
465 p_v based on the observation of strong PPD and failure rates upon paired stimulations at ISI of
466 20 ms (***Figure 2 and Figure 3—figure supplement 2***). Given that single AP-induced vesicular
467 release occurs from TS vesicles but not from LS vesicles, p_v in the present study indicates the
468 fusion probability of TS vesicles. From the same reasons, p_{occ} denotes the occupancy of
469 release sites by TS vesicles. Note that our study does not provide direct clue whether release
470 sites are occupied by LS vesicles that are not tapped by a single AP, although an increase in
471 the LS vesicle number may accelerate the recovery of TS vesicles. As suggested in Neher

472 (2024), even if the number of LS plus TS vesicles are kept constant, an increase in p_{occ}
473 (occupancy by TS vesicles) would be interpreted as an increase in 'vesicular release probability'
474 as in the previous studies (Stevens and Wesseling, 1999; Garcia-Perez and Wesseling, 2008)
475 as long as it was measured based on RRP_{hyper}.
476

477 *Progressive overfilling of docking sites*

478 Conventional models for facilitation assume an increase in p_v after an AP of RRP vesicles,
479 which had been in a low p_v or reluctant state at rest (Dittman et al., 2000; Turecek et al., 2016).
480 This facilitation model is unlikely to explain our results, because TS vesicles are predominantly
481 released not only at rest but also in the facilitated state during or after train stimulation, as
482 evidenced by the strong PPD (ISI, 25 ms) during a 5-Hz train (***Figure 2D-E***) and at different
483 intervals after a 40-Hz/30 pulse trains (***Figure 3D***). Moreover, the PPD (ISI, 25 ms) remained
484 pronounced during the early phase of facilitation (***Figure 7***), arguing against the possibility of
485 slowly increasing the p_v of reluctant vesicles. These results suggested that facilitation was
486 mediated by an activity-dependent progressive increase in occupancy of TS vesicles (TS
487 occupancy). Facilitation through an increase in TS occupancy has been termed frequency
488 facilitation, differentiating it from paired pulse facilitation that relies on a residual calcium-
489 dependent transient increase in the p_v of releasable vesicles (Neher, 2024).
490 Assuming an increase in TS occupancy, to attain a two-fold increase in EPSC (***Figure 1***), the
491 baseline occupancy of the docking sites by TS vesicles should be low, as estimated from the
492 V-M plot (c.a. 30% in ***Figure 3***). However, it is unclear whether the remaining docking sites

493 that are not occupied by TS vesicles are truly vacant or are occupied by reluctant LS vesicles
494 that are not released by the AP or AP trains. TS vesicles can be supplied by the transformation
495 of LS to TS vesicles, both of which reside at the same docking site (LS/TS model; reviewed in
496 Neher, 2024). Alternatively, TS vesicles can be supplied from a distinct replacement pool
497 (RS/DS model; reviewed in Silva et al., 2021). Further studies, including ultrastructural
498 analyses of active zones, are required to address this issue.
499 Given the crucial role of Syt7 in facilitation (***Figure 5***), the facilitation mechanisms are closely
500 related to how Syt7 mediates synaptic facilitation. Based on the slow kinetics of Syt7, previous
501 computational modeling studies have proposed that Syt7 may mediate short-term facilitation
502 through an activity-dependent increase in p_v (Turecek et al., 2016; Jackman and Regehr, 2017;
503 Turecek et al., 2017; Norman et al., 2023). The present study, however, found that both
504 facilitation and augmentation were mediated by overfilling of the release sites (***Figure 2 and***
505 ***Figure 3***). Moreover, Syt7-KD synapses displayed slower recovery of TS vesicles (***Figure 7***).
506 These results suggest that Syt7 is essential for activity-dependent overfilling of docking sites
507 with TS vesicles. Whereas the baseline EPSC was not altered (***Figure 1—figure supplement 3***),
508 and complementary changes in the number of docking sites and their baseline occupancy
509 were observed in Syt7 KD synapses (***Figure 6***). These results raise a possibility that Syt7 may
510 play a role in providing additional vacant docking sites that can be overfilled during facilitation.
511 It remains to be elucidated whether the decrease in the number of docking sites at Syt7 KD
512 synapses is related to the subcellular localization of Syt7 to the plasma membrane of the
513 active zone (Sugita et al., 2001; Vevea et al., 2021).
514

515 *STP model in light of known Ca^{2+} binding kinetics of Syt7*

516 Syt7 acts as an upstream Ca^{2+} sensor that facilitates activity-dependent replenishment (Liu et
517 al., 2014; Bacaj et al., 2015; Chen et al., 2017; Tawfik et al., 2021). The present study shows
518 that EPSCs are mediated by TS vesicles both at rest and during activity-dependent facilitation.
519 Releasable vesicles are homogeneous, and Syt7-dependent overfilling is responsible for the
520 activity-dependent enhancement of EPSCs. Thus, we tested whether slowly developing
521 facilitation could be replicated within the framework of a simple refilling model based on the
522 known Ca^{2+} binding kinetics of Syt7 (Brandt et al., 2012). To this end, we made following
523 assumptions: (1) a Ca^{2+}-dependent increase in the forward refilling rate (k_1) requires a full
524 Ca^{2+}-bound form of Syt7, to which multiple Ca^{2+} ions can bind (two or three Ca^{2+} ions on each
525 C2A and/or C2B domain) (Brandt et al., 2012; Chon et al., 2015; Voleti et al., 2017); (2)
526 sequential Ca^{2+} binding steps are synergistic through a cooperativity factor, *b*; (3) Syt7 senses
527 AP-induced local [Ca^{2+}] similar to that estimated at the calyx of Held (a Gaussian function with
528 a full width at half maximum value of 0.2 ms and a peak of 40 µM) (Wang et al., 2008); and
529 (4) residual [Ca^{2+}] follows a mono-exponential function with an amplitude of 1 µM and decay
530 time constant of 50 ms (Jackson and Redman, 2003).
531 Under these assumptions and the framework of the simple refilling model, slow and delayed
532 facilitation could be replicated by modeling k_1 as $k_1 = k_{1,b} + K_{1,max} \times$ [Syt7: n Ca^{2+}], where [Syt7:
533 n Ca^{2+}] represents the fraction of fully Ca^{2+}-bound Syt7 (***Figure 9A-C***). Syt7 was slowly
534 activated over the course of the stimulus train, suggesting that the cooperative binding of
535 multiple Ca^{2+} ions progressively increased the putative active form of Syt7 because of its slow
536 membrane binding/unbinding kinetics. Nevertheless, the late phase of facilitation at high

537 frequencies was predicted to be higher in the simulation than in the experiment. As expected,
538 based on the notion that sustained release during HFS is limited by site clearance in the active
539 zone (***Figure 4C***), the model/data discrepancy became more pronounced at higher
540 frequencies. Incorporating endocytic terms into the model may mitigate late-phase
541 discrepancies. Moreover, removal of the catalytic function of Syt7 in the model effectively
542 accounted for the complete loss of facilitation observed in Syt7 KD (***Figure 9D***).
543

544 *Conventional STF models involving cumulative increase in p_v of reluctant vesicles*

545 Conventional models for facilitation assume a post-AP residual Ca^{2+}-dependent step increase
546 in p_v of RRP (Dittman et al., 2000) or reluctant vesicles (Turecek et al., 2016). Given that p_v of
547 TS vesicles is close to one in the present study, an increase in p_v of TS vesicles cannot account
548 for facilitation. The possibility for activity-dependent increase in fusion probability of LS
549 vesicles (denoted as $p_{v,LS}$) should be considered in two ways depending on whether LS and TS
550 vesicles reside in distinct pools or in the same pool. Notably, strong PPD at short ISI implies
551 that $p_{v,LS}$ is near zero at the resting state. Whereas LS vesicles do not contribute to baseline
552 transmission, short-term facilitation (STF) may be mediated by cumulative increase in p_v of LS
553 vesicles that reside in a distinct pool. Because the increase in $p_{v,LS}$ during facilitation recruits
554 new release sites (increase in N), the variance of EPSCs should become larger as stimulation
555 frequency increases, resulting in upward deviation from a parabola in the V-M plane, as
556 shown in recent studies (Valera et al., 2012; Kobbersmed et al., 2020). This prediction is not
557 compatible with our results of V-M analysis (***Figure 3***), showing that EPSCs during STF fell on

558 the same parabola regardless of stimulation frequencies. Therefore, it is unlikely that an
559 increase in fusion probability of reluctant vesicles residing in a distinct release pool mediates
560 STF in the present study. For the latter case, in which LS and TS vesicles occupy in the same
561 release sites, it is hard to distinguish a step increase in fusion probability of LS vesicles from a
562 conversion of LS vesicles to TS. Nevertheless, our results do not support the possibility for a
563 gradual increase in $p_{v,LS}$ that occurs in parallel with STF. Strong PPD, indicative of high p_v, was
564 consistently found not only in the baseline (***Figure 2 and Figure 2—figure supplement 1***) but
565 also during post-tetanic augmentation phase (***Figure 3D***) and even during the early
566 development of facilitation (***Figure 2D-E and Figure 7***), arguing against the gradual increase
567 in $p_{v,LS}$. One may argue that STF may be mediated by a drastic step increase of $p_{v,LS}$ from zero
568 to one, but it is not distinguishable from conversion of LS to TS vesicles.
569

570 *Possible mechanisms underlying the depression-facilitation sequence*

571 Cooperative binding of multiple Ca^{2+} ions to Syt7 predicts delayed activation and a progressive
572 increase in vesicle refilling during train stimulations, resulting in delayed facilitation.
573 Combining this with a high p_v could replicate not only the slow facilitation at 5 Hz, but also
574 the unique depression-facilitation sequence observed at 40 Hz (***Figure 9***). As simulated by
575 Pulido and Marty (2018), delayed facilitation can be reproduced by a high p_v in combination
576 with a low baseline occupancy of replacement sites and subsequent Ca^{2+}-dependent refilling.
577 However, whether this model is also able to replicate slow facilitation at low frequencies
578 remains to be tested. An alternative, but not exclusive, possibility for delayed facilitation is

579 that the presynaptic global Ca^{2+} itself may undergo a slow buildup during a train due to the
580 saturation of endogenous Ca^{2+}-binding proteins.
581

582 *Facilitation requires not only Syt7, but also activation of PLC-DAG signaling*

583 To gain insight into the specific molecular mechanisms underlying the vesicle-loading
584 processes, we examined the effects of pharmacological inhibitors targeting PLC and DAG
585 (***Figure 4***). Both a PLC inhibitor and a DAG analog reduced facilitation and augmentation. This
586 suggests that the progressive overfilling of docking sites with TS vesicles is supported by the
587 PLC-DAG signaling pathway and probably downstream Munc13 (Rhee et al., 2002; Lou et al.,
588 2008). Phorbol esters have been recently shown to increase the TS fraction of docked vesicles
589 by enhancing vesicle priming without affecting Ca^{2+} transients or p_v (Taschenberger et al.,
590 2016; Aldahabi et al., 2022; Papantoniou et al., 2023; Aldahabi et al., 2024). In line with these
591 findings, signaling involving PLC and DAG may support Ca^{2+}-dependent overfilling of TS
592 vesicles by enhancing molecular priming processes.
593

594 *Roles of facilitation and augmentation in working memory and related tasks*

595 Previous theoretical studies have proposed that working memory in a recurrent network can
596 be maintained in the form of augmentation at synapses (Mongillo et al., 2008) and/or
597 persistent activity of neurons in a memory ensemble (Mongillo et al., 2012). The latter can be
598 supported by short-term facilitation of recurrent excitatory synapses or disparity in STP
599 between excitatory and inhibitory synapses (Mongillo et al., 2012; Yoon et al., 2020). However,

600 whether these short-term enhancements in synaptic efficacy contribute to working memory-
601 related behaviors has not been examined. tFC is a temporal associative learning task requiring
602 temporary retention of CS information during a trace period. The mPFC and hippocampus are
603 crucial for tFC, and tFC is interfered with by a load of working memory and attention
604 distraction, implying that the tFC shares the same neural substrate with other working
605 memory tasks (Raybuck and Lattal, 2014). In the present study, tFC in WT and Syt7 KD animals
606 revealed that Syt7 deficiency in the L2/3 PCs of the mPFC impaired the acquisition of trace
607 fear memory and reduced c-Fos expression associated with tFC training (***Figure 8***).
608 The acquisition of trace fear memory was impaired by inhibition of persistent activity in mPFC
609 during trace period (Gilmartin et al., 2013). The similar deficit observed in Syt7 KD animals is
610 consistent with the hypothesis that STF provides bi-stable ensemble activity in a recurrent
611 network (Mongillo et al., 2012). Nevertheless, alternative mechanisms may be responsible for
612 the behavioral deficit. Not only recurrent network but also long-range loop between the
613 mPFC and the mediodorsal (MD) thalamus play a critical role in maintaining persistent activity
614 within the mPFC especially for a delay period longer than 10 s (Bolkan et al., 2017). Prefrontal
615 L2/3 is heavily innervated by MD thalamus, and L2/3-PCs subsequently relay signals to L5
616 cortico-thalamic (CT) neurons (Collins et al., 2018). Given that L2/3 is an essential component
617 of the PFC-thalamic loop, loss of STF at recurrent synapses between L2/3 PCs may lead to
618 insufficient L2/3 inputs to L5 CT neurons and failure in the reverberant PFC-MD thalamic
619 feedback loop. Therefore, not only L2/3 recurrent network but also its output to downstream
620 network should be considered as a possible network mechanism underlying behavioral deficit
621 caused by Syt7 KD L2/3.

622 In summary, activity-dependent synaptic facilitation and augmentation at prelimbic L2/3
623 recurrent excitatory synapses can be attributed to overfilling of release sites with TS vesicles.
624 Given that the lack of short-term facilitation in L2/3 PCs impairs trace fear memory acquisition,
625 temporary maintenance of CS information during trace period may be supported by an
626 increase in the TS occupancy in presynaptic terminals of CS-representing neuronal ensembles.
627
628

629 ## Materials and Methods

630 *Animals/Subjects*

631 All experiments were carried out on Sprague-Dawley rats of either sex at p28-43. Rats were
632 maintained in temperature-controlled rooms on a constant 12 h light/12 h dark cycle and
633 were given access to water and food ad libitum. All animal procedures were approved and
634 performed in accordance with the Institutional Animal Care and Use Committee at Seoul
635 National University (SNU200522-1).

636

637 *In utero electroporation (IUE)*

638 Pregnant Sprague Dawley rats on embryonic day (E) 17.5 were deeply anesthetized with 5%
639 (v/v) isoflurane for the duration of surgery. The uterine horns were exposed by laparotomy
640 and wet with warm sterile phosphate-buffered saline (PBS). The plasmids (0.5-2 μg/μl)
641 together with the 0.01% fast green dye were injected into either the left or the right lateral
642 ventricle or bilateral ventricles of embryos through a thin glass capillary (Narishige PC-10).
643 The embryo's head was carefully held between the forceps-shaped electrodes of 10 mm
644 diameter (CUY65010; NEPAGENE, Japan). Electroporation pulses (50 V for 50 ms) were
645 delivered five times at intervals of 150 ms using a square-wave generator (ECM830; BEX,
646 United States). The uterine horns were placed back into the abdominal cavity and abdominal
647 muscles and skin were sutured. After the surgery, the animals were recovered under the
648 infrared lamp. For knockdown experiments in slice electrophysiology, the shRNA constructs
649 were co-electroporated with the pCAG-oChIEF-tdTomato, because of the consistent co-

650 expression of the two constructs in a significant proportion of the transfected cells in vivo
651 (Bony et al., 2013). Pups with robust fluorescence signals in the prefrontal cortex of both
652 hemispheres were used for behavior experiments.
653

654 *Preparation of vector constructs*

655 For an optic stimulation, pCAG-oChIEF-tdTomato was transfected by IUE. Short hairpin RNA
656 (shRNA) against Syt7 sequence (GATCTACCTGTCCTGGAAGAG) was expressed under the
657 control of an U6 promoter of pAAV-U6-GFP vector (Cell Biolabs, #VPK-413). This shRNA was
658 shown to effectively knockdown Syt7 in cell cultures and in vivo by previous reports from
659 more than one research group (Bacaj et al., 2013; Li et al., 2017). Scrambled control sequence
660 (TCGCATAGCGTATGCCGTT) was designed by shuffling the recognition region sequences and
661 a BLAST analysis confirmed that the control shRNA sequence had no target gene. For rescue
662 experiments, the cDNA for rat Syt7 (NM_021659) rendered resistant to the shRNA were
663 inserted in the KD vector and their expression was driven by the CAG promoter; the vector
664 also contained a self-cleaving P2A peptide sequence followed by EGFP, which ensures
665 visualization of transfected cells. All the constructs above were verified by DNA sequencing.
666 Plasmid DNA was purified and concentrated under endotoxin free conditions (Qiagen
667 EndoFree Maxi Kit).
668

669 *Slice preparation*

670 Acute brain slices were prepared by using a VT1200S Vibratome (Leica Microsystems) after
671 isoflurane anesthesia and decapitation. Coronal sections of the mPFC (300 µm in thickness)
672 were cut in ice-cold artificial cerebrospinal fluid (aCSF) composed of (in mM) 125 NaCl, 3.2
673 KCl, 25 $NaHCO_3$, 1.25 NaH_2PO_4, 20 D-glucose, 2 NaPyr, 1 $MgCl_2$, and 1.3 $CaCl_2$ (Yoon et al.,
674 2020), bubbled with 95% O_2 and CO_2 (pH = 7.3; 310 mOsm). Slices were allowed to recover
675 for a minimum of 30 minutes at 36 °C, and subsequently maintained at room temperature
676 until recording. Composition of aCSF was identical throughout the preparation, incubation,
677 and recording periods unless otherwise stated. For the recordings, the mPFC slices were
678 continuously perfused with oxygenated aCSF at a flow rate of 1.5 ml/min, and the
679 temperature was maintained at 31–32 °C using an in-line temperature controller (Warner
680 Instruments).

681

682 *Electrophysiology*

683 Whole-cell patch-clamp recordings were performed from pyramidal cells and fast-spiking
684 interneurons in layer 2/3 of the prelimbic mPFC. Neuronal subtypes were initially selected
685 based on morphology under visual guidance by using an upright microscope equipped with
686 infrared differential interference contrast (IR-DIC) optics (BX51WI, Olympus), and were
687 further identified by their electrophysiological properties (see ***Figure 1—figure supplement***
688 ***1***; van Aerde and Feldmeyer, 2015; Tremblay et al., 2016). To analyze these intrinsic
689 properties in current-clamp experiments, we measured the following parameters: (1) resting

690 membrane potential (RMP), (2) input resistance (R_{in}), (3) sag ratio, and (4) the F-I curve, which
691 plots firing frequencies (F) against the amplitude of injected currents (I). Both cell types
692 exhibited a low sag ratio below 0.1, consistent with findings from other studies (van Aerde
693 and Feldmeyer, 2015; Yoon et al., 2020). PCs and FSINs were easily distinguished by their
694 unique firing frequency, Rin, spike adaptation, RMP and morphological characteristics
695 including the shape of soma and the thickness of apical dendrites. For experiments involving
696 oChIEF-expressing neurons in WT or Syt7 KD rats, whole-cell recordings were performed from
697 the fluorescently labeled pyramidal neurons in layer 2/3 of the prelimbic cortex using suitable
698 filter sets. Patch pipettes (tip resistance of 2–3 MΩ) were pulled from borosilicate glass and
699 filled with (in mM) 130 K-gluconate, 8 KCl, 10 HEPES, 0.2 EGTA, 20 Na_2Pcr, 0.3 Na_2GTP, 4
700 MgATP. Intracellular solutions were adjusted to pH 7.25 and 300–310 mOsm. Neurons were
701 voltage clamped at −78 mV and series resistance (Rs) were continuously monitored during
702 the EPSCs recordings. Experiments were discarded before analysis if the Rs changed by 20%
703 or larger deviation of baseline value. Measurements were not corrected for Rs compensation,
704 bridge balance, or liquid junction potential. Electrophysiological data were low-pass-filtered
705 at 1 kHz (Bessel) and acquired at 20 kHz using a Multiclamp 700B amplifier paired with
706 Digidata 1440A digitizer and Clampex 10.2 software (Molecular Devices).
707

708 *Synaptic stimulation*

709 IUE resulted in sparse expression of channelrhodopsin (10-20%) (***Figure 1A***). Exploiting the
710 sparse expression, we employed a minimal optical stimulation method to activate a single or
711 very few excitatory synapses in layer 2/3. The optic minimal stimulation was performed by

712 our published protocol with minor modifications (Yoon et al., 2020). This approach aimed to
713 minimize the risk of synaptic contamination, which could arise from engaging extra terminals
714 that were initially inactive (depolarized below threshold) but became active by temporal
715 summation during high-frequency trains. It also helped prevent the buildup of depolarization
716 at the synaptic terminals, which might influence the probability of release, as noted by
717 (Jackman et al., 2014). To achieve this, we employed a collimated digital micromirror device
718 (DMD)-coupled LED (Polygon400; Mightex Systems) to confine 470 nm blue light to a small
719 area with a radius of approximately 3–8 µm (typically 3–4 µm), as measured at the focal plane
720 of a 60× water immersion objective [numerical aperture (NA) = 1.0; LUMPlanFL, Olympus]
721 (***Figure 1—figure supplement 3A***). To find the minimal stimulation area, the radius of
722 illumination area was increased from 2 µm by 50% at each step (***Figure 1—figure supplement***
723 ***3A***), and selected the smallest illumination area that elicited EPSCs. Setting the duration of
724 illumination between 3 and 5 ms (typically 5 ms), photostimulation onto oChIEF-expressing
725 cells reliably induced action potentials (APs) during 600-pulse trains (see ***Figure 1—figure***
726 ***supplement 2***).
727 STP at various stimulus frequencies (5, 10, 20, and 40 Hz) was examined using 20-pulse trains.
728 Trials of train stimulation were repeated with a prolonged interval of 30 s to avoid change in
729 baseline properties. We observed no systematic changes in the amplitudes of the first EPSC
730 of each train, nor did we find significant differences in the paired-pulse ratio (PPR) across
731 stimulation trials in the same cell. For each stimulus frequency, approximately ten to twenty
732 consecutive traces were collected and then averaged across trials to yield a mean EPSC trace.
733 For recovery experiments, two consecutive trains of 3 or 30 stimuli at 40 Hz, with varying time

734 intervals (0.1-10 s), were applied every 10 s or 60 s, respectively, at both excitatory synapses.
735 For 600-stimulus trains at 10Hz, the trial was delivered only once for each cell to avoid
736 possible after-effects caused by prolonged synaptic stimulation (Hirsch and Crepel, 1990).
737 Prior to the stimulus trains, the EPSCs were normalized to the mean amplitude of the baseline.
738 For the baseline measurements, paired pulses with various ISIs (20-200 ms) were delivered
739 every 3 s (1/3 Hz) at least 20 times.
740 For all recordings, picrotoxin (PTX, 10 µM) was included in the recording solution to isolate
741 glutamatergic responses. mPFC PC terminals were entirely glutamatergic as the application
742 of 6-cyano-7-nitroquinoxaline-2,3-dione (CNQX, 20 µM), an AMPA receptor antagonist,
743 completely abolished the monosynaptic events evoked by photostimulation. A low
744 concentration of PTX was employed to minimize the relieving effects on spike suppression
745 caused by blockade of GABAa receptors. We confirmed that no synaptic response was elicited
746 by electrical stimulation in the presence of both 10 µM PTX and 20 µM CNQX.
747 In ***Figure 1—figure supplement 4A***, 1 µM TTX (1 mM stock solution) and 0.1 mM 4-AP (500
748 mM stock solution) were added to the bath solution to block action potentials and restore
749 presynaptic glutamate release, respectively (***Figure 1—figure supplement 4***). In ***Figure 1—***
750 ***figure supplement 5A***, 50 µM of cyclothiazide, a positive allosteric modulator of the AMPA
751 receptors, was included to minimize rapid desensitization of the postsynaptic receptors. In
752 ***Figure 1—figure supplement 5B***, 0.5 mM kynurenate was added to bath solution to prevent
753 possible saturation of AMPA receptors, especially during maximal synaptic facilitation. For
754 pharmacological manipulations of synaptic vesicle dynamics (***Figure 4***), drugs related to
755 vesicle supply including U73122, OAG, LatB, EGTA-AM, and dynasore at indicated

concentrations were added to the recording solution during baseline measurements or PTA/recovery experiments (IBI = 0.5 s). Chemicals were from Sigma-Aldrich, Merck, or Tocris.

Measurements of quantal size

Experiments for measuring asynchronous release were performed as previously described (Yoon et al., 2020). In brief, we replaced extracellular Ca^{2+} entirely with 2 mM Sr^{2+} to induce asynchronous release. A single stimulus was delivered at 3-second intervals over 100 repetitions, and asynchronous release events were detected during a 100-ms window starting 25 ms after stimulus onset for each trial. The same procedure was also executed under sham conditions (0% light intensity) to serve as a control, thus mitigating contamination from nonspecific spontaneous events and potential errors associated with in the detection algorithm. q was determined as the mean value from the first Gaussian function after fitting the EPSC distribution with either a single or double Gaussian function (***Figure 3—figure supplement 1***).

Estimation of Ca^{2+} kinetics at axonal boutons

Cytosolic [Ca^{2+}] at single axonal boutons was estimated by employing the two-dye, dual-excitation wavelength technique as described by (Oheim et al., 1998). This method involves measuring the fluorescence ratio of a Ca^{2+}-sensitive dye to that of a Ca^{2+}-insensitive dye to correct for dye concentrations. We used Fluo-5F at concentrations of 150, 250, or 500 µM (dissociation constant, K_d = 2.3 µM) as the calcium indicator dye and Alexa Flour 555 (50 µM)

777 as the reference dye. The fluorophores were from Invitrogen. Both dyes were co-loaded into
778 presynaptic terminals of layer 2/3 pyramidal cells in mPFC through whole-cell patch clamp.
779 Before data acquisition, the dyes were allowed to diffuse to terminal boutons for at least 30
780 minutes after the patch break-in, a duration sufficient for the equilibrium of dye
781 concentrations between the soma and its axonal terminals.
782 Calcium imaging was performed by sequentially exciting Fluo-5F and AF555 at wavelengths
783 of 473 and 559 nm, respectively, using a confocal laser-scanning microscope (FV1200;
784 Olympus, Japan) equipped with a 60× water immersion objective (NA, 0.9; LUMPlanFl;
785 Olympus, Tokyo, Japan). Once a single axonal bouton was identified, lines for scanning were
786 drawn across boutons, oriented perpendicular to the axon (***Figure 2—figure supplement 2A-***
787 ***B***). After baseline fluorescence was measured, line scanning was proceeded while a single or
788 train APs were induced by applying current pulses. Upon stimulation, green fluorescence but
789 not red one increased along the vertical array of lines across the bouton (***Figure 2—figure***
790 ***supplement 2B-C***). Measurements were obtained under current-clamp conditions, with the
791 resting potential regularly monitored. The scanning speed was adjusted to 600-700 Hz by
792 controlling the line length. Line scan for measuring fluorescent transients in a bouton was
793 repeated at least 3 times, and then averaged to enhance the signal-to-noise ratio. To mitigate
794 photobleaching, minimal intensity of the laser power and maximal pinhole size were used.
795 Emitted light was filtered through 490/590 or 575/675 bandpass filters before detection by
796 photomultiplier tubes for green or red fluorescence, respectively.

797 Fluorescence measurements were converted to $[Ca^{2+}]_i$ using the ratio of background-
798 subtracted fluorescence ($F = F_0 - F_b$) from two dyes. The fluorescence ratio ($R = F_{green}/F_{red}$) in
799 data traces were converted to $[Ca^{2+}]_i$ using the following equation:

800 $$[Ca^{2+}]_i = K_d \times (R - R_{min}) / (R_{max} - R). \quad (1)$$

801 Calibration parameters were obtained using an in-cell calibration protocol (Helmchen, 2011),
802 wherein the minimum (R_{min}) and maximum ratio (R_{max}) values were established through the
803 use of intracellular solutions containing 10 mM EGTA or 10 mM $[Ca^{2+}]$, respectively.
804 When Ca^{2+} is extruded with a rate constant, γ, after an AP-induced short pulse of Ca^{2+} influx
805 to a single compartment, $[Ca^{2+}]_i$ initially rises to A_{Ca} and then undergoes a mono-exponential
806 decay with a time constant (τ_{Ca}). Under this framework, A_{Ca} and τ_{Ca} depend on Ca^{2+} binding
807 ratios of endo- and exogenous Ca^{2+} buffers (denoted as κ_S and κ_B, respectively) as following
808 equations (Neher, 1995; Kim et al., 2003):

809 $$1/A_{Ca} = (1 + \kappa_S + \kappa_B) / \Delta[Ca^{2+}]_T. \quad (2)$$

810 $$\tau_{Ca} = (1 + \kappa_S + \kappa_B) / \gamma. \quad (3)$$

811 , where $\Delta[Ca^{2+}]_T$ is an increment in total $[Ca^{2+}]$ (free plus bound) elicited by an AP. Ca^{2+} binding
812 ratio indicates the ratio of concentration changes in the Ca^{2+}-buffer complex relative to free
813 $[Ca^{2+}]$ change, and linearized κ_B is calculated from the dye concentration and the change from
814 $[Ca^{2+}]_1$ to $[Ca^{2+}]_2$ as follows:

815 $$\kappa_B = \Delta[CaB] / \Delta[Ca^{2+}] = [B]_t K_d / [([Ca^{2+}]_1 + K_d)([Ca^{2+}]_2 + K_d)]. \quad (4)$$

816 The total dye concentration, $[B]_t$, was taken as [Fluo-5F] in the patch pipette. With κ_B
817 determined from Equation 4 and τ_{Ca} from the decay of a Ca^{2+} transient, κ_S can be estimated

818 by plotting τ versus κ_B and applying a linear fit to the plot, which gives the x-intercept as -(1 +

819 κ_S). Once determined, κ_S can be used to calculate $\Delta[Ca^{2+}]_T$.

820

821 *Optimization of k_1 and p_v from failure rates*

822 Let n_0 = the number of docked SVs before arrival of a first AP; n_1 = the number of docked SVs

823 remaining after a first AP (i.e. n_0 - n_1 vesicles are released); n_2 = the number of docked SVs

824 just before arrival of a 2nd AP (ISI = 20 ms; ***Figure 3—figure supplement 2***). If the number of

825 release sites (N), forward and reverse rates for vesicle docking (k_1 and b_1, respectively), mean

826 release site occupancy (p_{occ}) and vesicular fusion probability upon an AP (p_v) are given, we can

827 predict $P(n_0, n_1, n_2)$, the probability for $[n_0, n_1, n_2]$, as following steps.

828 1) Probability for a synapse harbouring n_0 docked SVs just before arrival of a first AP is

829 calculated as:

830 $$P(n_0) = C(N, n_1)\, p_{occ}^{n0} \times (1 - p_{occ})^{(N-n0)}.$$

831 2) Probability that n_1 vesicles remain after a first AP when the initial number of docked SVs is

832 n_0 $[P(n_1|n_0)]$ is calculated as:

833 $$P(n_1|n_0) = C(n_0, n_1) \times (1-p_v)^{n1} \times p_v^{(n0-n1)}, \text{ if } n_0 \geq n_1 ,$$

834 $$P(n_1|n_0) = 0, \text{ if } n_0 < n_1.$$

835 3) When forward and backward rate constants are k_1 and b_1, respectively, probability that n_2

836 vesicles are docked just before arrival of a 2nd AP when n_1 SVs remain after a 1st AP (Δt = 20

837 ms) $[P(n_2 \mid n_1)]$ is predicted as follows: Assuming that docking and undocking follow a Poisson

838 process,

$$P(n_2 \mid n_1) = C(N - n_1, n_2 - n_1)\,[1 - \exp(-k_1\,\Delta t)]^{(n2 - n1)}, \text{ if } n_2 > n_1 .$$

$$P(n_2 \mid n_1) = C(n_1, n_1 - n_2)\,[1 - \exp(-b_1\,\Delta t)]^{(n1 - n2)}, \text{ if } n_2 < n_1 .$$

$$P(n_2 \mid n_1) = \exp[-n_1\,k_1\,\Delta t]\,\exp[-n_1\,b_1\,\Delta t], \text{ if } n_2 = n_1 .$$

4) Combining probabilities calculated from above three steps, we can calculate $P(n_0, n_1, n_2)$:

$$P(n_0, n_1, n_2) = P(n_0) \times P(n_1|n_0) \times P(n_2|n_1)$$

5) Once $P(n_0, n_1, n_2)$ is given, we can predict probability for double failure (P_{00}) and probability for the 1st success and the 2nd failure (P_{10}) as:

$$P_{00} = \Sigma_{n0=0..N}\,\Sigma_{n1 = n0}\,\Sigma_{n2 = 0..N}\quad p(n_0, n_1, n_2)\,(1 - p_v)^{n2} .$$

$$P_{10} = \Sigma_{n0=0..N}\,\Sigma_{n1 \neq n0}\,\Sigma_{n2 = 0..N}\quad p(n_0, n_1, n_2)\,(1 - p_v)^{n2} .$$

6) Probability for the 1st failure and the 2nd success (P_{01}) and probability for double success (P_{11}) were calculated as:

$$P_{01} = P(F_1) - P(F_1, F_2)$$

$$P_{11} = P(S_1) - P(S_1, F_2)$$

, in which $P(F_1)$ and $P(S_1)$ are probability for the 1st failure and the 1st success, respectively, and these are calculated as:

$$P(F_1) = P(n_0)\,P(F_1 \mid n_0) = \Sigma_{n0=0..N}\,P(n_0)\,(1 - p_v)^{n0} ,$$

$$P(S_1) = 1 - P(F_1).$$

To optimize k_1 and p_v, we used the Matlab routine, *fmincon*, in which the sum of squared errors (= observed value minus predicted value) was set as a cost function to be minimized. Lower and upper bounds for k_1 and p_v were set as [4, 8] and [0.8, 1], respectively. Release probability (p_r) was calculated from the observed 1st failure rate, $P(F_1)$, as

$$p_r = 1 - [P(F_1)]^{(1/N)}$$

N was assumed to be six as shown in ***Figure 3***. Other parameters (b_1, and p_{occ}) were set according to following relationships:

$$p_{occ} = p_r / p_v .$$

$$b_1 = k_1 (1 - p_{occ})/p_{occ} .$$

Calculation of probability for double failure

Double failure probability, P_{00}, can be more easily predicted. By the Bayes rule,

$$P(F_1, F_2, n_1) = P(F_2 \mid n_1, F_1)\, P(F_1 \mid n_1)\, P(n_1).$$

, where F_1 and F_2 means 1st and 2nd failure. Moreover, and $n_0 = n_1$ because of the 1st failure. Thus, the probability for two consecutive failures can be calculated as:

$$P(F_1, F_2) = \Sigma_{n1=0..N}\, P(F_2 \mid n_1, F_1)\, P(F_1 \mid n_1)\, P(n_1).$$

$P(F_1)$ and N are observed values. For calculation in ***Figure 3—figure supplement 2***, k_1 and p_v were set free variables. Other parameters were set under the following constrains: $P(F_1) = (1 - p_r)^N$, $p_r = p_v\, p_{occ}$, and $p_{occ} = k_1 / (k_1 + b_1)$.

Behavioral tests

Trace fear conditioning: For trace fear conditioning (tFC) (Gilmartin et al., 2013), individual rats were placed in the training chamber (30.5 x 25.4 x 30.5 cm; Coulbourn Instruments) consisting of metal grid floor connected to an electrical stimulator (H10-11R-TC-SF, Coulbourn Instruments) for delivery of a footshock. After a 5 min habituation period, rats received five pairings of a 20 s tone conditioned stimulus (CS, 2.5 kHz, 75 dB), followed by empty 20s trace

882 period and a unconditioned stimulus (US; 1 s, 0.7 mA footshock) with a pseudorandom inter-
883 trial interval (ITI) of 240 ± 20 s. During this training session, rats learned to associate the
884 auditory CS with the shock US. The next day, the rats were tested for memory of CS-US trace
885 association (called tone test). The acquisition of fear learning, often indicated by the extent
886 of freezing to the CS, was assessed in a novel chamber (a white hexagonal enclosure) in a
887 dimly lit room. During this tone (or retrieval) test, rats were first allowed to explore the new
888 context for 5 min (habituation), followed by twelve 20 s CS presentations with a variable ITI
889 of 120 ± 20 s. This entire session was repeated on the next day for assessment of extinction
890 learning. Identities of the chambers were also determined with the presence of distinct odors;
891 the training and testing chambers were cleaned with 70% ethanol and 1% acetic acid
892 respectively before and after each session. For all experimental sessions, the activity of
893 animals in the chambers was recorded at 30 frames per second using the EthoVision XT
894 (Noldus Information Technology, Wageningen, Netherlands), and stored as a video file. The
895 freezing behavior, defined as behavioral immobility other than respiratory movement, was
896 assessed using an open-source video analysis pipeline ezTrack (Pennington et al., 2019). The
897 percentage of freezing was calculated as a total duration of freezing divided by the total
898 duration of observation.
899 **Elevated Plus Maze**: Elevated plus maze (EPM) test was performed using a plus-shaped
900 apparatus elevated 60 cm above the ground. The maze consisted of two open arms (50 x 10
901 x 0.5 cm (H)), two closed arms (50 x 10 x 40 cm (H)) and a center area (10 x 10 cm). Rats were
902 individually placed on the center area, facing an open arm, and the path of the animal was
903 recorded with a video camera for 5 min. We analyzed the total distance traveled for 5 min

904 and time spent in each arm. Animals were tracked offline using the open-source tracking
905 system ezTrack (Pennington et al., 2019).
906 **Open field test**: Open field exploration test (OFT) was performed in an open field apparatus
907 in a dimly lit room. The open field consisted of a white plastic board (1.20 m in diameter)
908 surrounded by white plastic walls (50 cm in height). Individual rats were placed in a center
909 zone (0.6 m in diameter), and allowed to freely explore the apparatus for 10 min. Time spent
910 in the center zone and total distance traveled were analyzed for initial 5 min. Animals were
911 tracked offline using the open-source tracking system ezTrack (Pennington et al., 2019).
912

913 *Histology and immunohistochemistry*

914 At the end of the behavioral experiments, rats were anesthetized using isoflurane inhalation
915 and transcardially perfused with PBS followed by 4% paraformaldehyde (PFA, T&I, Korea).
916 Brains were extracted and post-fixed in 4% PFA solution for 24 h. Perfused brains were sliced
917 at 100 μm for estimation of GFP expression or 50 μm for immunohistochemistry. For analysis
918 of c-Fos expression, rats were returned to their home cages immediately after the training
919 session and perfused approximately 90 minutes later (Arime and Akiyama, 2017). Brains were
920 then cryopreserved, frozen, and sectioned coronally. Immunofluorescence staining was
921 conducted on free-floating slices using a rabbit monoclonal anti c-fos (1:1000, Cell Signaling
922 Technology, cat# 2250s) and mouse monoclonal anti-GAD67 (1:500, Millipore, cat# mab5406).
923 Fluorescent secondary antibodies included Cy5-conjugated goat anti-rabbit IgG (1:1000,
924 Abcam, cat# ab97077) and Cy3-conjugated goat anti-mouse IgG (1:1000, Abcam, cat#
925 ab97035). Brain slices were permeabilized and blocked with PBS containing 0.5% Triton X-100

926 and 5% normal goat serum (NGS) for 1h at room temperature. Slices were incubated
927 overnight at 4 °C with primary antibodies, followed by 4 h incubation with secondary
928 antibodies at room temperature. Slices were then mounted with Antifading Mounting
929 medium (Abcam, cat# ab104139). Confocal images were acquired using a Leica TCS SP8
930 microscope set to the same laser intensity and acquisition parameters to compare the
931 immunosignals in sections from Scr and Syt7 KD groups. For cell counting and colocalization,
932 fluorescent protein-positive cells were automatically quantified with spot-detection
933 algorithms in Imaris 9.5 (Oxford instruments).
934

935 *Data analysis*

936 Data were analyzed and presented using ClampFit (Molecular Devices), Igor Pro
937 (Wavemetrics), MATLAB (Mathworks), and Prism (GraphPad). Data points and error bars
938 represent the mean ± standard error of the mean. All statistical analyses were conducted
939 using two-tailed comparisons. Sample sizes and statistical tests for each group are detailed in
940 the figure legends.
941

942 *Numerical integration of the simple refilling model*

943 This model posits reversible docking of vesicles at finite release sites (N_{max}) with forward (k_1)
944 and reverse rate constants (b_1) (Hosoi et al., 2007; Neher and Sakaba, 2008).

$$\underset{b_1}{\overset{k_1}{\rightleftarrows}} n \xrightarrow{p_v}$$

945

946 According to this scheme, $dn/dt = k_1\ u - b_1\ n - p_v\ n\ \delta(t - t_{AP})$, where u is the number of
947 unoccupied sites (= $N_{max} - n$); t_{AP} is the timing of AP firing; and δ is the Dirac delta function.
948 The p_v was assumed to be unity (***Figure 3—figure supplement 2***). The sum of basal k_1 (= $k_{1,b}$)
949 and b_1 was be estimated as 23/s from the dependence PPR on ISIs (***Figure 3—figure***
950 ***supplement 2Ab***). From the baseline occupancy of 0.3 and $p_{occ} = k_{1,b} / (k_{1,b} + b_1)$, we could
951 estimate baseline k_1 and b_1 as 6.9/s, and 16.1/s, respectively. Ca^{2+}- and Syt7-dependent
952 increase of k_1 was modeled as $k_1 = k_{1,b} + K_{1,max}$ [Syt7: n Ca^{2+}], where [Syt7: n Ca^{2+}] represents
953 the fraction of full Ca^{2+}-bound Syt7. For deterministic simulations, we time-integrated a set
954 of differential equations for each model using Euler methods with a time step of 1 ms. All
955 calculations were performed on the platform of Matlab (R2022b, Mathworks, USA).

956

957 ## Acknowledgements

958 We thank Dr. E. Neher and Dr. A. Marty for critical reading of this manuscript and
959 invaluable comments.

960

961 ## Author contributions

962 All experiments were carried out at cell physiology lab under Y.K and S.H.L's supervision.
963 Conception or design of the work: J.S. and S.H.L. Acquisition, analysis or interpretation of data

964 for the work: J.S, Y.K. and L.S.H. Drafting the work or revising it critically for important
965 intellectual content: J.S., S.Y.L, Y.K. and L.S.H.
966

967 Funding

968 This study was supported by grants from the National Research Foundation of Korea (RS-
969 2024-333669 to S-H. Lee; 2021R1I1A1A01059646 to Y. Kim), and Seoul National University
970 Hospital (2024).
971
972

973 ## References

974 Aldahabi M, Neher E, Nusser Z (2024) Different states of synaptic vesicle priming explain
975 target cell type-dependent differences in neurotransmitter release. Proc Natl Acad Sci
976 U S A 121:e2322550121.
977 Aldahabi M, Balint F, Holderith N, Lorincz A, Reva M, Nusser Z (2022) Different priming states
978 of synaptic vesicles underlie distinct release probabilities at hippocampal excitatory
979 synapses. Neuron 110:4144-4161 e4147.
980 Arime Y, Akiyama K (2017) Abnormal neural activation patterns underlying working memory
981 impairment in chronic phencyclidine-treated mice. PLoS One 12:e0189287.
982 Bacaj T, Wu D, Burre J, Malenka RC, Liu X, Sudhof TC (2015) Synaptotagmin-1 and -7 Are
983 Redundantly Essential for Maintaining the Capacity of the Readily-Releasable Pool of
984 Synaptic Vesicles. PLoS Biol 13:e1002267.
985 Bacaj T, Wu D, Yang X, Morishita W, Zhou P, Xu W, Malenka RC, Sudhof TC (2013)
986 Synaptotagmin-1 and synaptotagmin-7 trigger synchronous and asynchronous phases
987 of neurotransmitter release. Neuron 80:947-959.
988 Baeg EH, Kim YB, Huh K, Mook-Jung I, Kim HT, Jung MW (2003) Dynamics of population code
989 for working memory in the prefrontal cortex. Neuron 40:177-188.
990 Bolkan SS, Stujenske JM, Parnaudeau S, Spellman TJ, Rauffenbart C, Abbas AI, Harris AZ,
991 Gordon JA, Kellendonk C (2017) Thalamic projections sustain prefrontal activity during
992 working memory maintenance. Nat Neurosci 20:987-996.
993 Bony G, Szczurkowska J, Tamagno I, Shelly M, Contestabile A, Cancedda L (2013) Non-
994 hyperpolarizing GABAB receptor activation regulates neuronal migration and neurite
995 growth and specification by cAMP/LKB1. Nat Commun 4:1800.
996 Brandt DS, Coffman MD, Falke JJ, Knight JD (2012) Hydrophobic contributions to the
997 membrane docking of synaptotagmin 7 C2A domain: mechanistic contrast between
998 isoforms 1 and 7. Biochemistry 51:7654-7664.
999 Chen C, Satterfield R, Young SM, Jr., Jonas P (2017) Triple Function of Synaptotagmin 7
1000 Ensures Efficiency of High-Frequency Transmission at Central GABAergic Synapses.
1001 Cell Rep 21:2082-2089.
1002 Chon NL, Osterberg JR, Henderson J, Khan HM, Reuter N, Knight JD, Lin H (2015) Membrane
1003 Docking of the Synaptotagmin 7 C2A Domain: Computation Reveals Interplay between
1004 Electrostatic and Hydrophobic Contributions. Biochemistry 54:5696-5711.
1005 Collins DP, Anastasiades PG, Marlin JJ, Carter AG (2018) Reciprocal Circuits Linking the
1006 Prefrontal Cortex with Dorsal and Ventral Thalamic Nuclei. Neuron 98:366-379 e364.
1007 Dittman JS, Kreitzer AC, Regehr WG (2000) Interplay between facilitation, depression, and
1008 residual calcium at three presynaptic terminals. J Neurosci 20:1374-1385.
1009 Dobrunz LE, Huang EP, Stevens CF (1997) Very short-term plasticity in hippocampal synapses.
1010 Proceedings of the national academy of sciences 94:14843-14847.
1011 Fields RD, Eshete F, Stevens B, Itoh K (1997) Action potential-dependent regulation of gene
1012 expression: temporal specificity in ca2+, cAMP-responsive element binding proteins,
1013 and mitogen-activated protein kinase signaling. J Neurosci 17:7252-7266.

1014 Fujisawa S, Amarasingham A, Harrison MT, Buzsaki G (2008) Behavior-dependent short-term
1015 assembly dynamics in the medial prefrontal cortex. Nat Neurosci 11:823-833.
1016 Garcia-Perez E, Wesseling JF (2008) Augmentation controls the fast rebound from depression
1017 at excitatory hippocampal synapses. J Neurophysiol 99:1770-1786.
1018 Gilmartin MR, Miyawaki H, Helmstetter FJ, Diba K (2013) Prefrontal activity links
1019 nonoverlapping events in memory. J Neurosci 33:10910-10914.
1020 Guzowski JF, Timlin JA, Roysam B, McNaughton BL, Worley PF, Barnes CA (2005) Mapping
1021 behaviorally relevant neural circuits with immediate-early gene expression. Curr Opin
1022 Neurobiol 15:599-606.
1023 Hallermann S, Silver RA (2013) Sustaining rapid vesicular release at active zones: potential
1024 roles for vesicle tethering. Trends Neurosci 36:185-194.
1025 Hansel D, Mato G (2013) Short-term plasticity explains irregular persistent activity in working
1026 memory tasks. J Neurosci 33:133-149.
1027 Hass CA, Glickfeld LL (2016) High-fidelity optical excitation of cortico-cortical projections at
1028 physiological frequencies. J Neurophysiol 116:2056-2066.
1029 Haucke V, Neher E, Sigrist SJ (2011) Protein scaffolds in the coupling of synaptic exocytosis
1030 and endocytosis. Nat Rev Neurosci 12:127-138.
1031 Helmchen F (2011) Calibration protocols for fluorescent calcium indicators. Cold Spring Harb
1032 Protoc 2011:980-984.
1033 Hempel CM, Hartman KH, Wang XJ, Turrigiano GG, Nelson SB (2000) Multiple forms of short-
1034 term plasticity at excitatory synapses in rat medial prefrontal cortex. J Neurophysiol
1035 83:3031-3041.
1036 Hirsch JC, Crepel F (1990) Use-dependent changes in synaptic efficacy in rat prefrontal
1037 neurons in vitro. J Physiol 427:31-49.
1038 Holler S, Kostinger G, Martin KAC, Schuhknecht GFP, Stratford KJ (2021) Structure and
1039 function of a neocortical synapse. Nature 591:111-116.
1040 Holmgren C, Harkany T, Svennenfors B, Zilberter Y (2003) Pyramidal cell communication
1041 within local networks in layer 2/3 of rat neocortex. J Physiol 551:139-153.
1042 Hosoi N, Sakaba T, Neher E (2007) Quantitative analysis of calcium-dependent vesicle
1043 recruitment and its functional role at the calyx of Held synapse. J Neurosci 27:14286-
1044 14298.
1045 Jackman SL, Regehr WG (2017) The Mechanisms and Functions of Synaptic Facilitation.
1046 Neuron 94:447-464.
1047 Jackman SL, Beneduce BM, Drew IR, Regehr WG (2014) Achieving high-frequency optical
1048 control of synaptic transmission. J Neurosci 34:7704-7714.
1049 Jackman SL, Turecek J, Belinsky JE, Regehr WG (2016) The calcium sensor synaptotagmin 7 is
1050 required for synaptic facilitation. Nature 529:88-91.
1051 Jackson MB, Redman SJ (2003) Calcium dynamics, buffering, and buffer saturation in the
1052 boutons of dentate granule-cell axons in the hilus. J Neurosci 23:1612-1621.
1053 Kim MH, Lee SH, Park KH, Ho WK, Lee SH (2003) Distribution of K+-dependent Na+/Ca2+
1054 exchangers in the rat supraoptic magnocellular neuron is polarized to axon terminals.
1055 J Neurosci 23:11673-11680.

1056 Kobbersmed JRL, Grasskamp AT, Jusyte M, Böhme MA, Ditlevsen S, Sørensen JB, Walter AM
1057 (2020) Rapid regulation of vesicle priming explains synaptic facilitation despite
1058 heterogeneous vesicle:Ca2+ channel distances. eLife 9:e51032.
1059 Kusick GF, Chin M, Raychaudhuri S, Lippmann K, Adula KP, Hujber EJ, Vu T, Davis MW,
1060 Jorgensen EM, Watanabe S (2020) Synaptic vesicles transiently dock to refill release
1061 sites. Nat Neurosci 23:1329-1338.
1062 Lee HR, Choi SH, Lee SH (2024) Differential involvement of mitochondria in post-tetanic
1063 potentiation at intracortical excitatory synapses of the medial prefrontal cortex. Cereb
1064 Cortex 34.
1065 Lee JS, Ho WK, Lee SH (2010) Post-tetanic increase in the fast-releasing synaptic vesicle pool
1066 at the expense of the slowly releasing pool. J Gen Physiol 136:259-272.
1067 Lee JS, Ho WK, Lee SH (2012) Actin-dependent rapid recruitment of reluctant synaptic vesicles
1068 into a fast-releasing vesicle pool. Proc Natl Acad Sci U S A 109:E765-774.
1069 Li YC, Chanaday NL, Xu W, Kavalali ET (2017) Synaptotagmin-1- and Synaptotagmin-7-
1070 Dependent Fusion Mechanisms Target Synaptic Vesicles to Kinetically Distinct
1071 Endocytic Pathways. Neuron 93:616-631 e613.
1072 Lin JY, Lin MZ, Steinbach P, Tsien RY (2009) Characterization of engineered channelrhodopsin
1073 variants with improved properties and kinetics. Biophys J 96:1803-1814.
1074 Lin KH, Taschenberger H, Neher E (2022) A sequential two-step priming scheme reproduces
1075 diversity in synaptic strength and short-term plasticity. Proc Natl Acad Sci U S A
1076 119:e2207987119.
1077 Liu H, Bai H, Hui E, Yang L, Evans CS, Wang Z, Kwon SE, Chapman ER (2014) Synaptotagmin 7
1078 functions as a Ca2+-sensor for synaptic vesicle replenishment. Elife 3:e01524.
1079 Lou X, Korogod N, Brose N, Schneggenburger R (2008) Phorbol esters modulate spontaneous
1080 and Ca2+-evoked transmitter release via acting on both Munc13 and protein kinase C.
1081 J Neurosci 28:8257-8267.
1082 Macia E, Ehrlich M, Massol R, Boucrot E, Brunner C, Kirchhausen T (2006) Dynasore, a cell-
1083 permeable inhibitor of dynamin. Dev Cell 10:839-850.
1084 Malagon G, Miki T, Tran V, Gomez LC, Marty A (2020) Incomplete vesicular docking limits
1085 synaptic strength under high release probability conditions. Elife 9.
1086 Markram H, Wang Y, Tsodyks M (1998) Differential signaling via the same axon of neocortical
1087 pyramidal neurons. Proc Natl Acad Sci U S A 95:5323-5328.
1088 Martinetti LE, Bonekamp KE, Autio DM, Kim HH, Crandall SR (2022) Short-Term Facilitation of
1089 Long-Range Corticocortical Synapses Revealed by Selective Optical Stimulation. Cereb
1090 Cortex 32:1932-1949.
1091 Miki T, Malagon G, Pulido C, Llano I, Neher E, Marty A (2016) Actin- and Myosin-Dependent
1092 Vesicle Loading of Presynaptic Docking Sites Prior to Exocytosis. Neuron 91:808-823.
1093 Mongillo G, Barak O, Tsodyks M (2008) Synaptic theory of working memory. Science
1094 319:1543-1546.
1095 Mongillo G, Hansel D, van Vreeswijk C (2012) Bistability and spatiotemporal irregularity in
1096 neuronal networks with nonlinear synaptic transmission. Phys Rev Lett 108:158101.
1097 Neher E (1995) The use of fura-2 for estimating Ca buffers and Ca fluxes. Neuropharmacology
1098 34:1423-1442.

1099 Neher E (2010) What is Rate-Limiting during Sustained Synaptic Activity: Vesicle Supply or the
1100 Availability of Release Sites. Front Synaptic Neurosci 2:144.
1101 Neher E (2024) Interpretation of presynaptic phenotypes of synaptic plasticity in terms of a
1102 two-step priming process. J Gen Physiol 156.
1103 Neher E, Sakaba T (2008) Multiple roles of calcium ions in the regulation of neurotransmitter
1104 release. Neuron 59:861-872.
1105 Neher E, Brose N (2018) Dynamically Primed Synaptic Vesicle States: Key to Understand
1106 Synaptic Short-Term Plasticity. Neuron 100:1283-1291.
1107 Norman CA, Krishnakumar SS, Timofeeva Y, Volynski KE (2023) The release of inhibition model
1108 reproduces kinetics and plasticity of neurotransmitter release in central synapses.
1109 Commun Biol 6:1091.
1110 Oheim M, Naraghi M, Muller TH, Neher E (1998) Two dye two wavelength excitation calcium
1111 imaging: results from bovine adrenal chromaffin cells. Cell Calcium 24:71-84.
1112 Otsuka T, Kawaguchi Y (2009) Cortical inhibitory cell types differentially form intralaminar and
1113 interlaminar subnetworks with excitatory neurons. J Neurosci 29:10533-10540.
1114 Ozdemir AT, Lagler M, Lagoun S, Malagon-Vina H, Lasztoczi B, Klausberger T (2020)
1115 Unexpected Rule-Changes in a Working Memory Task Shape the Firing of Histologically
1116 Identified Delay-Tuned Neurons in the Prefrontal Cortex. Cell Rep 30:1613-1626 e1614.
1117 Pan B, Zucker RS (2009) A general model of synaptic transmission and short-term plasticity.
1118 Neuron 62:539-554.
1119 Papantoniou C, Laugks U, Betzin J, Capitanio C, Ferrero JJ, Sanchez-Prieto J, Schoch S, Brose
1120 N, Baumeister W, Cooper BH, Imig C, Lucic V (2023) Munc13- and SNAP25-dependent
1121 molecular bridges play a key role in synaptic vesicle priming. Sci Adv 9:eadf6222.
1122 Pennington ZT, Dong Z, Feng Y, Vetere LM, Page-Harley L, Shuman T, Cai DJ (2019) ezTrack:
1123 An open-source video analysis pipeline for the investigation of animal behavior. Sci
1124 Rep 9:19979.
1125 Pulido C, Marty A (2018) A two-step docking site model predicting different short-term
1126 synaptic plasticity patterns. J Gen Physiol 150:1107-1124.
1127 Raybuck JD, Lattal KM (2014) Bridging the interval: theory and neurobiology of trace
1128 conditioning. Behav Processes 101:103-111.
1129 Reyes A, Sakmann B (1999) Developmental switch in the short-term modification of unitary
1130 EPSPs evoked in layer 2/3 and layer 5 pyramidal neurons of rat neocortex. J Neurosci
1131 19:3827-3835.
1132 Rhee JS, Betz A, Pyott S, Reim K, Varoqueaux F, Augustin I, Hesse D, Sudhof TC, Takahashi M,
1133 Rosenmund C, Brose N (2002) Beta phorbol ester- and diacylglycerol-induced
1134 augmentation of transmitter release is mediated by Munc13s and not by PKCs. Cell
1135 108:121-133.
1136 Ritzau-Jost A, Jablonski L, Viotti J, Lipstein N, Eilers J, Hallermann S (2018) Apparent calcium
1137 dependence of vesicle recruitment. J Physiol 596:4693-4707.
1138 Ritzau-Jost A, Delvendahl I, Rings A, Byczkowicz N, Harada H, Shigemoto R, Hirrlinger J, Eilers
1139 J, Hallermann S (2014) Ultrafast action potentials mediate kilohertz signaling at a
1140 central synapse. Neuron 84:152-163.
1141 Rozov A, Burnashev N, Sakmann B, Neher E (2001) Transmitter release modulation by
1142 intracellular Ca2+ buffers in facilitating and depressing nerve terminals of pyramidal

1143 cells in layer 2/3 of the rat neocortex indicates a target cell-specific difference in
1144 presynaptic calcium dynamics. J Physiol 531:807-826.
1145 Sakaba T, Neher E (2003) Involvement of actin polymerization in vesicle recruitment at the
1146 calyx of Held synapse. J Neurosci 23:837-846.
1147 Scheuss V, Schneggenburger R, Neher E (2002) Separation of presynaptic and postsynaptic
1148 contributions to depression by covariance analysis of successive EPSCs at the calyx of
1149 Held synapse. J Neurosci 22:728-739.
1150 Silva M, Tran V, Marty A (2021) Calcium-dependent docking of synaptic vesicles. Trends
1151 Neurosci 44:579-592.
1152 Silva M, Tran V, Marty A (2024) A maximum of two readily releasable vesicles per docking site
1153 at a cerebellar single active zone synapse. Elife 12.
1154 Stevens CF, Wesseling JF (1999) Augmentation is a potentiation of the exocytotic process.
1155 Neuron 22:139-146.
1156 Sugita S, Han W, Butz S, Liu X, Fernandez-Chacon R, Lao Y, Sudhof TC (2001) Synaptotagmin
1157 VII as a plasma membrane Ca(2+) sensor in exocytosis. Neuron 30:459-473.
1158 Taschenberger H, Woehler A, Neher E (2016) Superpriming of synaptic vesicles as a common
1159 basis for intersynapse variability and modulation of synaptic strength. Proc Natl Acad
1160 Sci U S A 113:E4548-4557.
1161 Tawfik B, Martins JS, Houy S, Imig C, Pinheiro PS, Wojcik SM, Brose N, Cooper BH, Sorensen
1162 JB (2021) Synaptotagmin-7 places dense-core vesicles at the cell membrane to
1163 promote Munc13-2- and Ca(2+)-dependent priming. Elife 10.
1164 Thomson AM, Lamy C (2007) Functional maps of neocortical local circuitry. Frontiers in
1165 neuroscience 1:48.
1166 Tran V, Silva M, Marty A (2023) Prioritized docking of synaptic vesicles provided by a rapid
1167 recycling pathway. iScience 26:106366.
1168 Tremblay R, Lee S, Rudy B (2016) GABAergic Interneurons in the Neocortex: From Cellular
1169 Properties to Circuits. Neuron 91:260-292.
1170 Turecek J, Jackman SL, Regehr WG (2016) Synaptic Specializations Support Frequency-
1171 Independent Purkinje Cell Output from the Cerebellar Cortex. Cell Rep 17:3256-3268.
1172 Turecek J, Jackman SL, Regehr WG (2017) Synaptotagmin 7 confers frequency invariance onto
1173 specialized depressing synapses. Nature 551:503-506.
1174 Valera AM, Doussau F, Poulain B, Barbour B, Isope P (2012) Adaptation of granule cell to
1175 Purkinje cell synapses to high-frequency transmission. J Neurosci 32:3267-3280.
1176 van Aerde KI, Feldmeyer D (2015) Morphological and physiological characterization of
1177 pyramidal neuron subtypes in rat medial prefrontal cortex. Cereb Cortex 25:788-805.
1178 Vandael D, Borges-Merjane C, Zhang X, Jonas P (2020) Short-Term Plasticity at Hippocampal
1179 Mossy Fiber Synapses Is Induced by Natural Activity Patterns and Associated with
1180 Vesicle Pool Engram Formation. Neuron 107:509-521 e507.
1181 Vevea JD, Kusick GF, Courtney KC, Chen E, Watanabe S, Chapman ER (2021) Synaptotagmin 7
1182 is targeted to the axonal plasma membrane through gamma-secretase processing to
1183 promote synaptic vesicle docking in mouse hippocampal neurons. Elife 10.
1184 Voleti R, Tomchick DR, Sudhof TC, Rizo J (2017) Exceptionally tight membrane-binding may
1185 explain the key role of the synaptotagmin-7 C(2)A domain in asynchronous
1186 neurotransmitter release. Proc Natl Acad Sci U S A 114:E8518-E8527.

1187 Wang LY, Neher E, Taschenberger H (2008) Synaptic vesicles in mature calyx of Held synapses
1188 sense higher nanodomain calcium concentrations during action potential-evoked
1189 glutamate release. J Neurosci 28:14450-14458.
1190 Wu LG, Chan CY (2022) Multiple Roles of Actin in Exo- and Endocytosis. Front Synaptic
1191 Neurosci 14:841704.
1192 Yau JO, McNally GP (2023) The Rescorla-Wagner model, prediction error, and fear learning.
1193 Neurobiol Learn Mem 203:107799.
1194 Yoon JY, Lee HR, Ho WK, Lee SH (2020) Disparities in Short-Term Depression Among Prefrontal
1195 Cortex Synapses Sustain Persistent Activity in a Balanced Network. Cereb Cortex
1196 30:113-134.
1197 Zucker RS, Regehr WG (2002) Short-term synaptic plasticity. Annu Rev Physiol 64:355-405.
1198

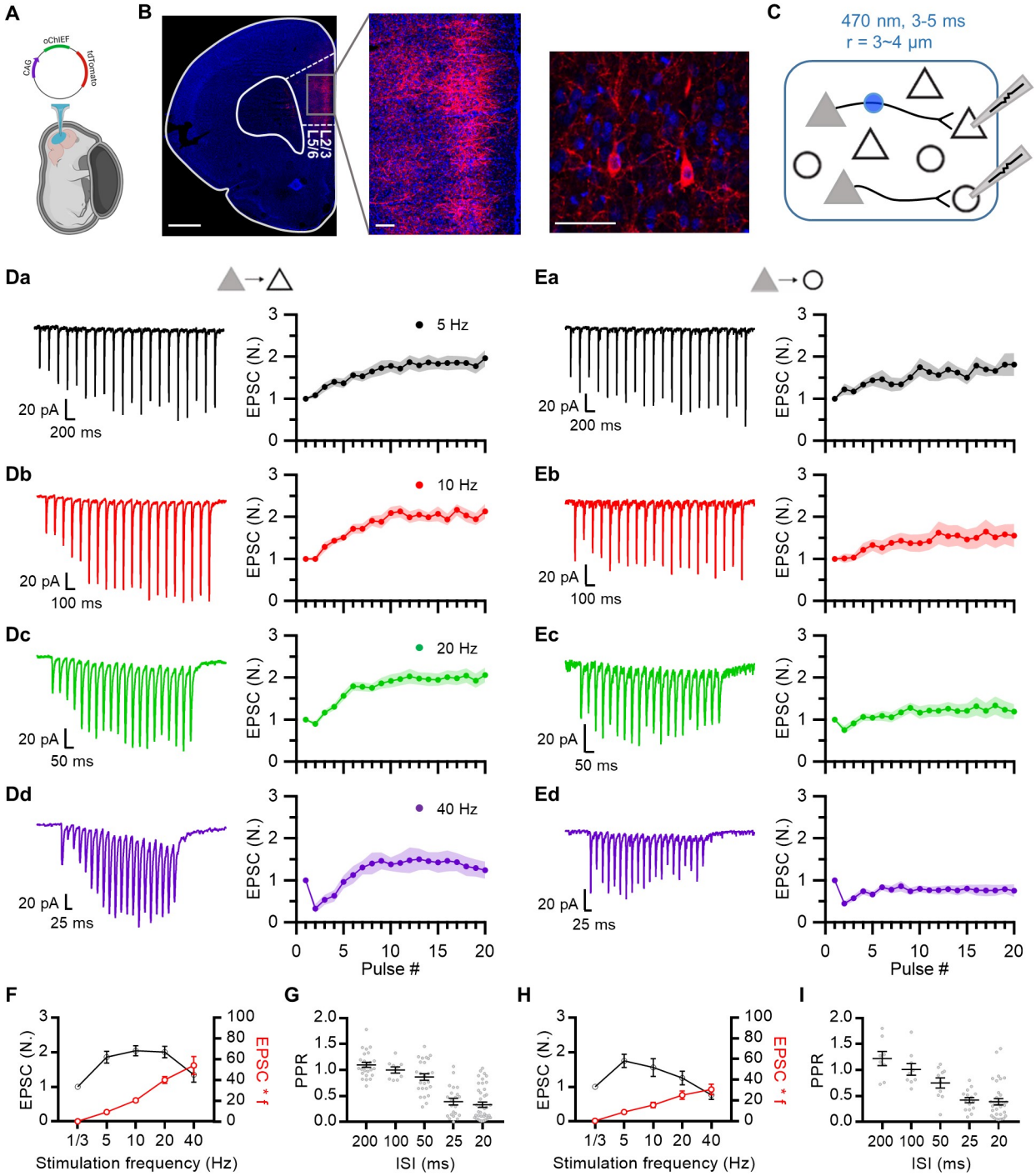

1 **Figure 1. Frequency-dependence of short-term synaptic plasticity at prelimbic L2/3**

2 **excitatory synapses.**

(**A**) In utero electroporation following injection of the plasmid (CAG-oChIEF-tdTomato) into the ventricle of an embryo (E17.5). (**B**) Representative images showing specific expression of oChIEF-tdTomato in L2/3 pyramidal cells after IUE. The red fluorescence of tdTomato clearly visualizes oChIEF-expressing cell bodies in L2/3 and axons in L5. Scale bar: 1 mm, 100 μm, 50 μm from left to right. (**C**) Recording schematic showing photostimulation of oChIEF-expressing axon fibers of transfected PCs (*filled triangles*) and a whole-cell recording from non-transfected PCs (*empty triangles*) or FSINs (*empty circles*). A collimated DMD-coupled LED was used to confine the area of excitation (typically 3–4 μm in diameter) to a small region (*blue circle*) near the soma. (**D, E**) Representative traces for EPSCs averaged over 10 trials at each frequency (*left*) and average amplitudes of baseline-normalized EPSCs (*right*) during 20-pulse trains at frequencies from 5 to 40 Hz at PC-PC (*D*; n = 12, 9, 21, 10 cells for 5, 10, 20, 40 Hz, respectively) and PC-FSIN (*E*; n = 8, 9, 10, 10) synapses. Each data point was normalized to the average of the first EPSC. (**F**) Baseline-normalized amplitudes of steady-state EPSCs ($EPSC_{ss}$; *black symbols*) and synaptic efficacy ($EPSC_{ss} \times f$; *red symbols*) as a function of stimulation frequency (*f*) at PC–PC synapses. $EPSC_{ss}$ was measured from the average of last 5 EPSCs from the 20-pulse trains (n = 12, 9, 21, 10). (**G**) Paired pulse ratio (PPR) as a function of inter-spike intervals (n = 25, 9, 25, 22, 43 for 200, 100, 50, 25, 20 ms ISI, respectively) at PC-PC synapses. (**H**) $EPSC_{ss}$ and synaptic efficacy at PC-FSIN (n = 8, 9, 10, 10). (**I**) PPR at PC-FSIN (n = 8, 9, 10, 15, 34). *Gray symbols*, individual data.

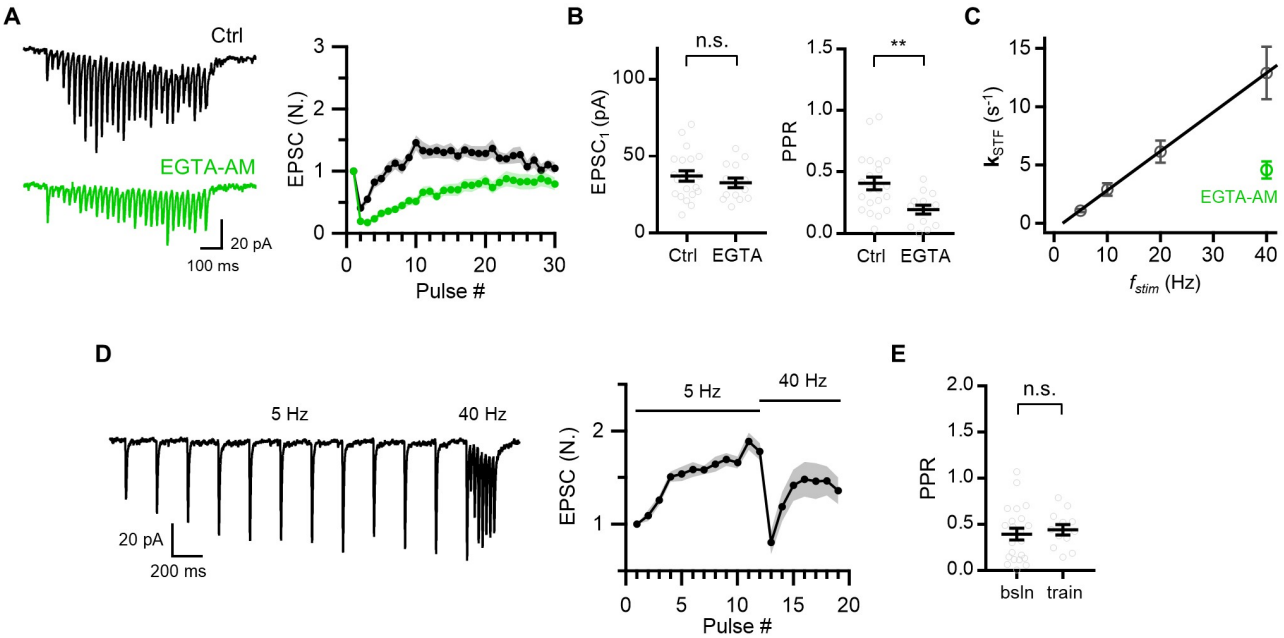

Figure 2. Delayed facilitation results from slow activation of Ca^{2+}-dependent vesicle replenishment at a constantly high vesicular fusion probability

(**A**) Representative traces (*left*) and mean baseline-normalized amplitudes (*right*) of EPSCs evoked by 30-pulse trains at 40 Hz in control (n = 21; *black*) and in the presence of 50 µM EGTA-AM (n = 14; *green*). (**B**) Mean values for the first EPSC amplitude ($EPSC_1$, *left*) and PPR (*right*) from the experiments displayed in (A). *Gray symbols*, individual data. (**C**) Plot of rate constants for short-term facilitation ($\mathbf{k}_{STF}$) as a function of stimulation frequency (f_{stim}), showing a linear relationship. The linear regression line (*black*) is shown fitted to $\mathbf{k}_{STF}$ values, estimated from ***Figure 1***. (**D**) Representative EPSC traces (*left*) and average of baseline-normalized EPSCs (*right*) evoked by 12-pulse stimulation at 5 Hz, followed by 40 Hz 7-pulse train (n = 12). Note that slowly developing facilitation was converted to rapid facilitation after strong PPD. (**E**) Mean values for PPR at 40 Hz. The baseline PPR was reproduced from ***Figure 1G*** and the PPR during 5 Hz train was calculated as (13th EPSC) / (12th EPSC). *Gray symbols*, individual data. All statistical data are represented as mean ± S.E.M.; n.s. = not significant; **, $P < 0.01$; unpaired t-test.

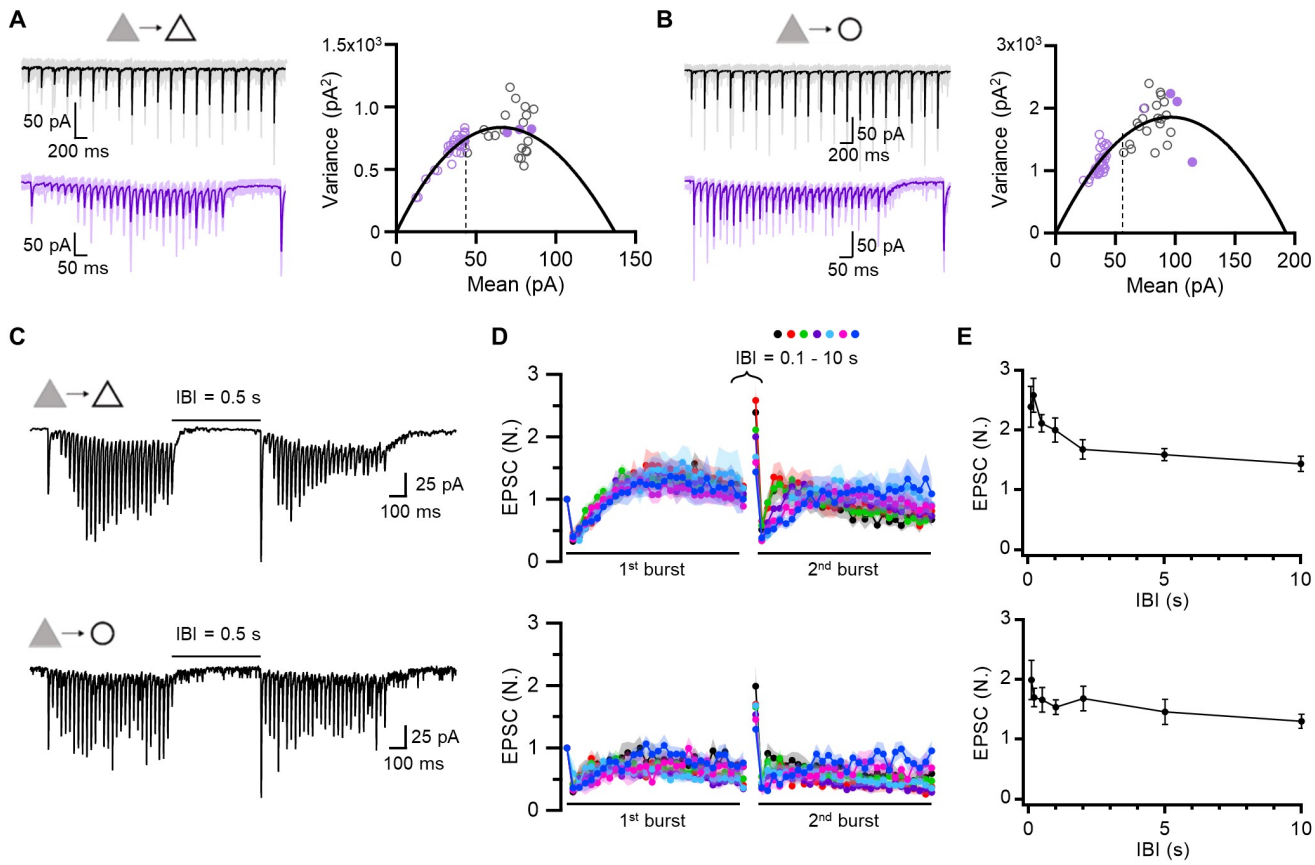

Figure 3. Low baseline occupancy of release sites and its increase during facilitation and post-tetanic augmentation

(**A, B**) *Left*, Representative EPSCs evoked by 5 and 40 Hz train stimulation (*black*, 5 Hz; *purple*, 40 Hz). *Right*, Variance-mean plots of EPSCs amplitude from averaged EPSCs recorded at PC-PC (A; n = 12, 17 for 5 and 40 Hz, respectively) and PC-FSIN (B; n = 8, 10) synapses. The data were fitted using multiple-probability fluctuation analysis (MPFA). Error bars are omitted for clarity. The 1st EPSC of 5 Hz train (*broken line*) was used to estimate the resting level of p_{occ}. *Filled circles* were measured from post-tetanic augmented EPSCs (*A*, n = 12, 12, 9; *B*, n = 7, 7, 7 for 0.1, 0.2, 0.5 s IBIs, respectively). (**C-E**) Post-tetanic augmentation (PTA) experiments at PC-PC (*top*) and PC-FSIN (*bottom*) synapses. (**C**) Representative traces for EPSCs evoked by double 40 Hz train stimulations separated by 0.5 s. (**D**) Mean baseline-normalized amplitudes of EPSCs evoked by double 40 Hz trains at different inter-burst intervals (IBIs, 0.1, 0.2, 0.5, 1, 2, 5, 10 s). *Upper*, PC-PC synapse (n = 12, 12, 21, 11, 11, 16, 11 from short to long IBIs,

respectively). *Lower*, PC-FSIN synapse (n = 10, 9, 8, 9, 9, 7, 9). (**E**) PTA time course. The baseline-normalized amplitudes of 1st EPSC from the 2nd train were plotted as a function of IBIs.

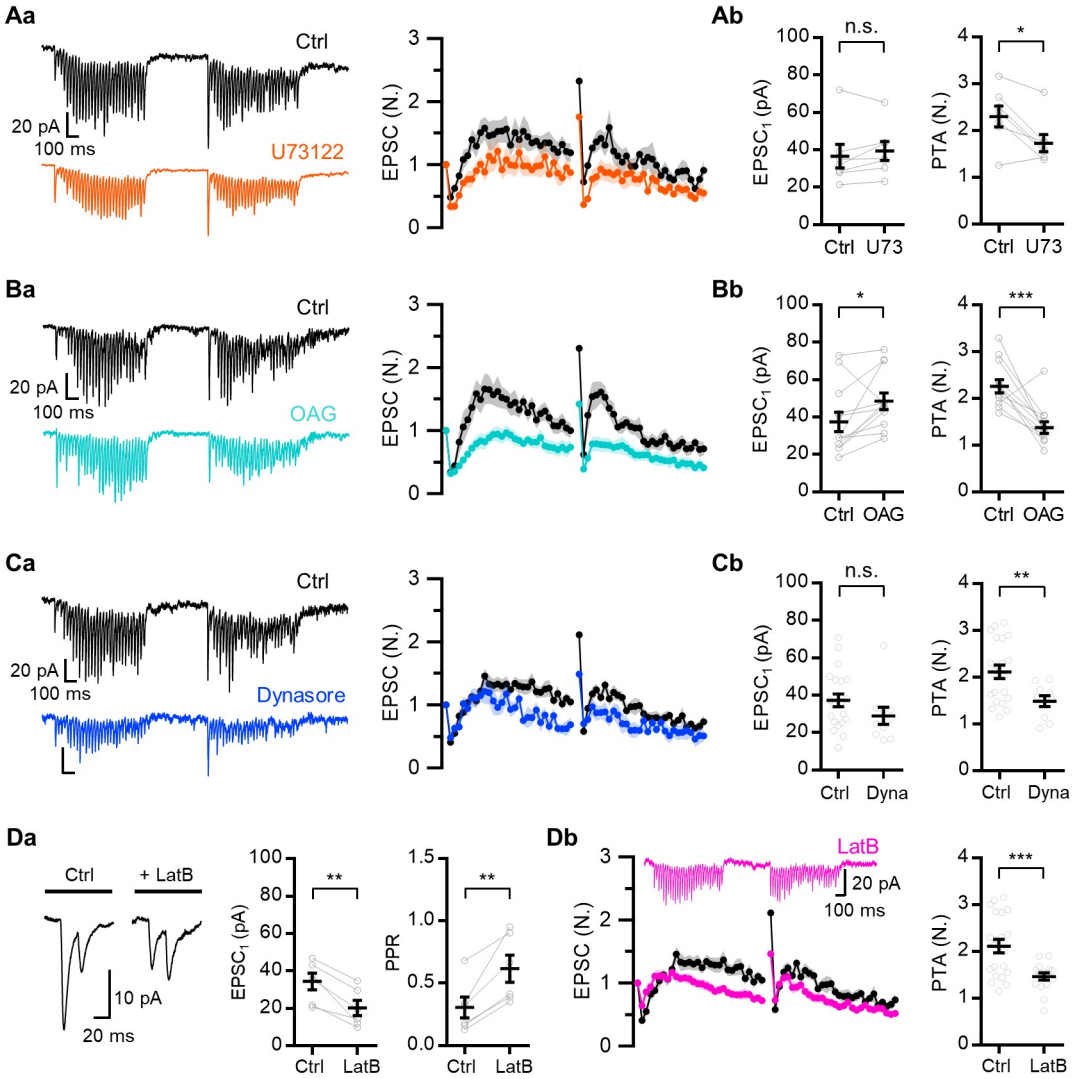

Figure 4. Pharmacological experiments reveal specific molecular mechanisms underlying vesicle loading processes

(**A-C**) (**a**) Representative EPSC traces (*left*) and mean baseline-normalized EPSCs (*right*) evoked by double 40 Hz train stimulations separated by 0.5 s inter-burst interval (IBI) in control and in the presence of 5 µM U73122 (*Aa*, n = 7, *orange*), 20 µM OAG (*Ba*, n = 12, *cyan*) or 100 µM dynasore (*Ca*, n = 10, *blue*). (**b**) Mean values for baseline EPSCs ($EPSC_1$, *left*) and augmentation (*right*) from the experiments shown in corresponding *a* panel. (**Da**) Representative EPSC traces evoked by paired pulses (*left*) and mean values for baseline EPSC amplitude (*middle*) and PPR (*right*) before and after applying 20 µM LatB (n = 6). (**Db**) Representative EPSC traces

66 (*left, upper*) and average of normalized EPSCs (*left, lower*) evoked by double 40 Hz train
67 stimulation separated by 0.5 s in control (n = 21) and in 20 µM LatB conditions (n = 16; *pink*).
68 *Right*, Mean values for augmentation in control and LatB conditions. *Gray symbols*, individual
69 data. All statistical data are represented as mean ± S.E.M., *, $P < 0.05$; **, $P < 0.01$; ***, $P <$
70 0.001; unpaired or paired t-test; n.s. = not significant.
71
72

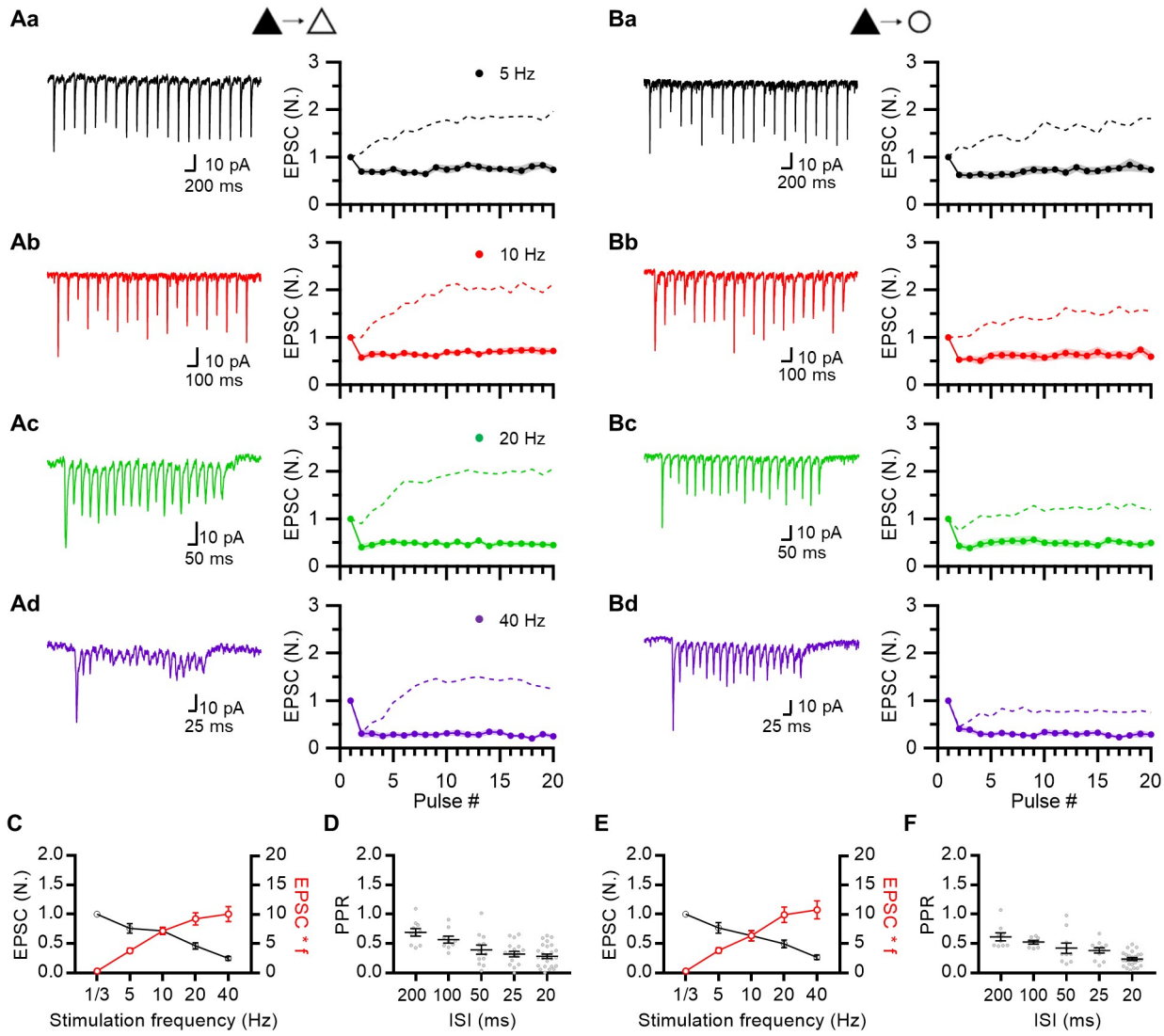

73 **Figure 5. STF at both types of local excitatory synapses is abolished by Syt7 KD**

74 (**A, B**) Representative EPSC traces (*left*) and mean baseline-normalized amplitudes of EPSCs
75 (*right*) evoked by 20-pulse trains at 5 to 40 Hz. STP was measured at PC-PC (*A*; n = 10, 9, 12,
76 9) and PC-FSIN (*B*; n = 9, 8, 10, 9) synapses, in which presynaptic Syt7 transcripts were
77 depleted (Syt7 KD). Syt7 KD pyramidal cells are indicated as *black triangles* on the top. For
78 comparison, STP in WT synapses is reproduced from ***Figure 1*** (*dotted lines*). Same frequency
79 color codes were used as in ***Figure 1***. (**C**) Baseline-normalized amplitudes of steady-state EPSC
80 ($EPSC_{ss}$; *black symbols*) and synaptic efficacy ($EPSC_{ss} \times f$; *red symbols*) as a function of

81 stimulation frequency (*f*) at PC-PC synapses. $EPSC_{ss}$ was defined as the average of last 5 EPSC
82 amplitudes from 20-pulse trains. (**D**) PPR as a function of inter-spike intervals (n = 10, 9, 12,
83 18, 26). (**E**) $EPSC_{ss}$ and synaptic efficacy at PC-FSIN synapses. (**F**) PPR at PC-FSIN synapses (n =
84 9, 8, 10, 12, 24). *Gray symbols*, individual data.
85
86

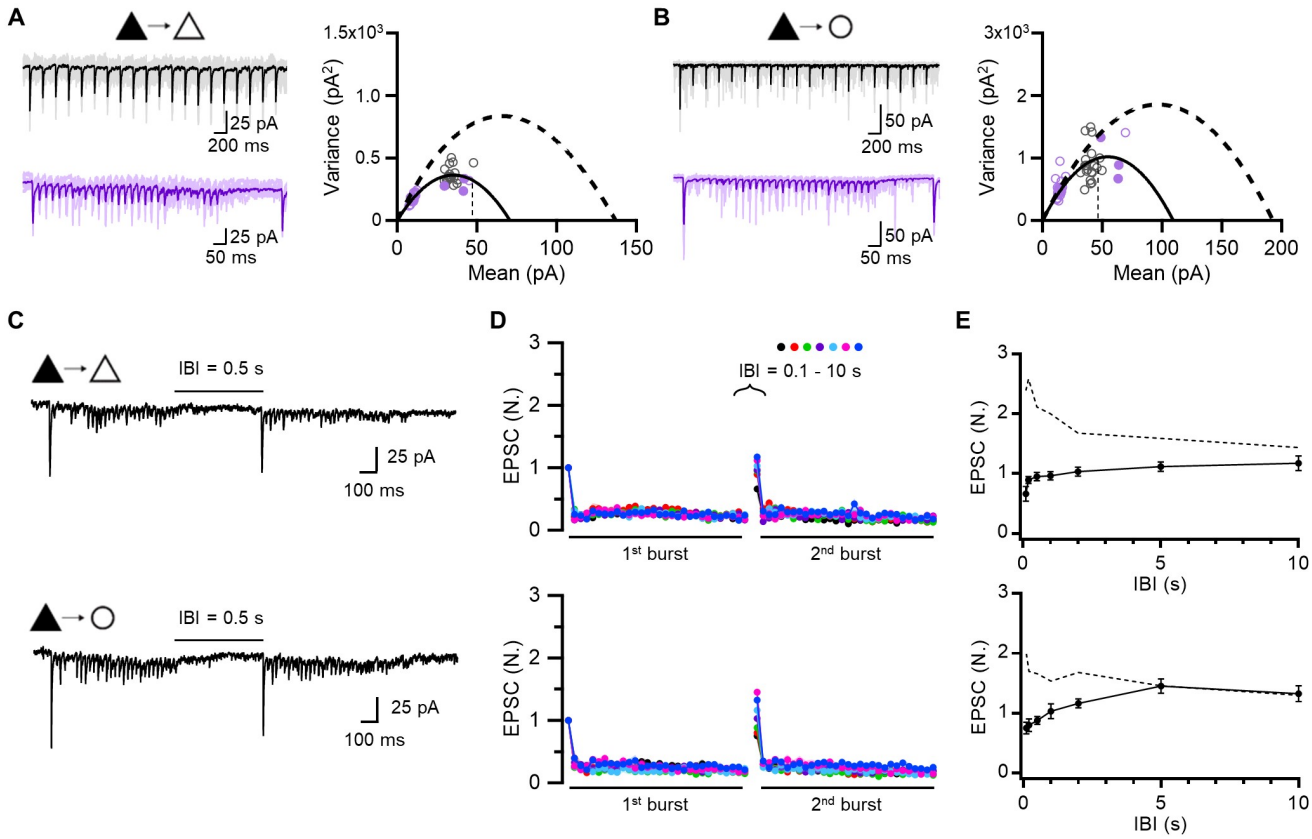

Figure 6. Syt7 KD synapses exhibit complementary changes in the number of release sites and their vesicle occupancy

(**A, B**) *Left*, Representative traces of EPSCs evoked by 5 and 40 Hz train stimulations (*black*, 5 Hz; *purple*, 40 Hz). *Right*, Variance-mean plots of EPSCs amplitude from averaged EPSCs recorded at PC-PC (*A*; n = 9, 15, 12, 10, 9) and PC-FSIN (*B*; n = 4, 14, 10, 9, 8) synapses in which presynaptic Syt7 has been knocked down. The data were fitted using MPFA and error bars are omitted for clarity. The mean 1st EPSC amplitude of 5 Hz train (*vertical broken line*) was used for estimation of baseline p_{occ}. Dashed parabolas indicate MPFA fits to variance-mean plot of WT synapses reproduced from *Figure 3*. (**C-E**) Recovery experiments at PC-PC (*top*) and PC-FSIN (*bottom*) synapses in which presynaptic Syt7 was knocked-down. (**C**) Representative EPSCs evoked by double 40 Hz train stimulations separated by 0.5 s. (**D**) Mean baseline-normalized amplitudes of EPSCs evoked by double 40 Hz trains at PC-PC (n = 12, 10, 9, 9, 10, 9, 8) and PC-FSIN (n = 10, 9, 10, 11, 8, 9, 10) synapses at different interburst intervals (IBIs).

100 (**E**) Recovery time course. Baseline-normalized amplitudes of 1st EPSC from the 2nd burst were
101 plotted as a function of various IBIs. *Dotted lines* indicate augmented EPSCs in the WT
102 reproduced from ***Figure 3***.
103
104

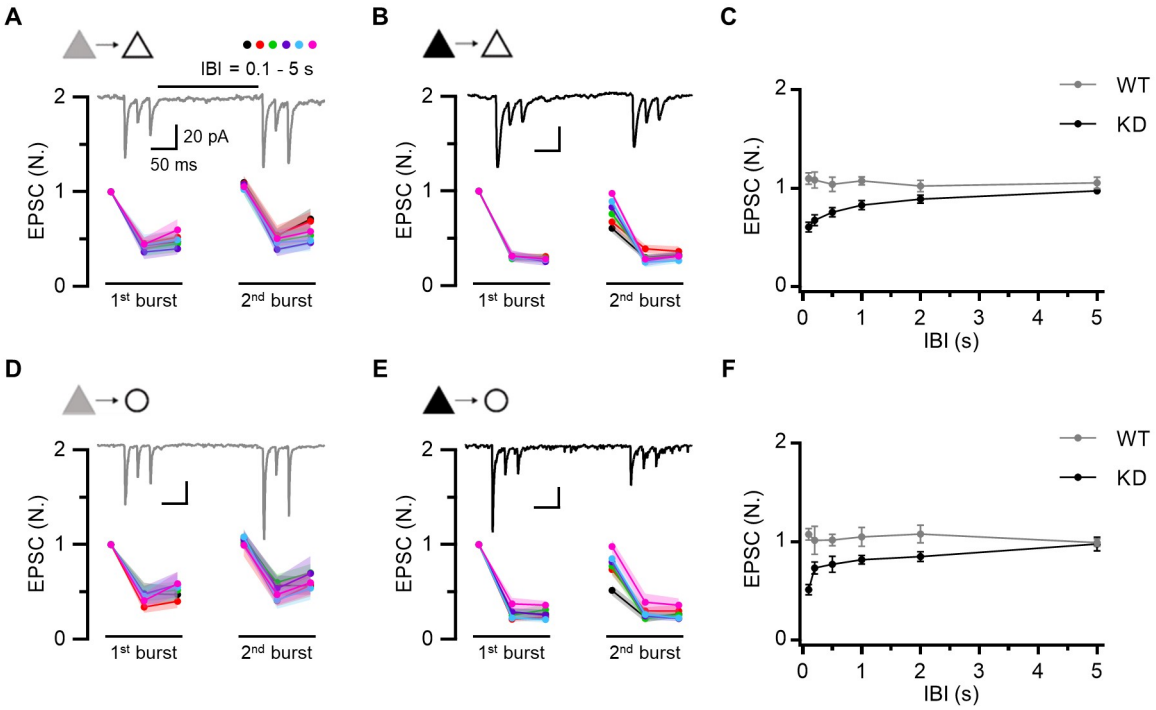

105 **Figure 7. Recovery of TS vesicles following depletion is accelerated by Syt7**

106 (**A-C**). Recovery experiments at PC-PC synapses in WT (*A*) and Syt7 KD (*B*). Mean baseline-
107 normalized amplitudes of EPSCs evoked by two consecutive 3-pulse 40 Hz trains in WT (n =
108 16, 13, 11, 11, 11, 9 from short to long IBIs, respectively) and KD (n = 13, 11, 12, 8, 10, 11)
109 synapses at different IBIs (0.1, 0.2, 0.5, 1, 2, 5 s). *Inset*, representative traces of EPSCs evoked
110 by two consecutive 3-pulse 40 Hz train stimulations separated by 0.2 s. (**D-F**). Recovery
111 experiments at PC-FSIN synapses in WT (*D*) and Syt7 KD (*E*). Mean baseline-normalized
112 amplitudes of EPSCs evoked by two consecutive 3-pulse 40 Hz trains in WT (n = 9, 11, 11, 9,
113 10, 13) and KD (n = 9, 12, 9, 7, 10, 9) synapses at different IBIs. *Inset*, representative traces of
114 EPSCs evoked by two consecutive 3-pulse 40 Hz train stimulations separated by 0.2 s. (**C, F**)
115 Recovery time course. Baseline-normalized amplitudes of 1st EPSC from the 2nd burst were
116 plotted as a function of various IBIs.

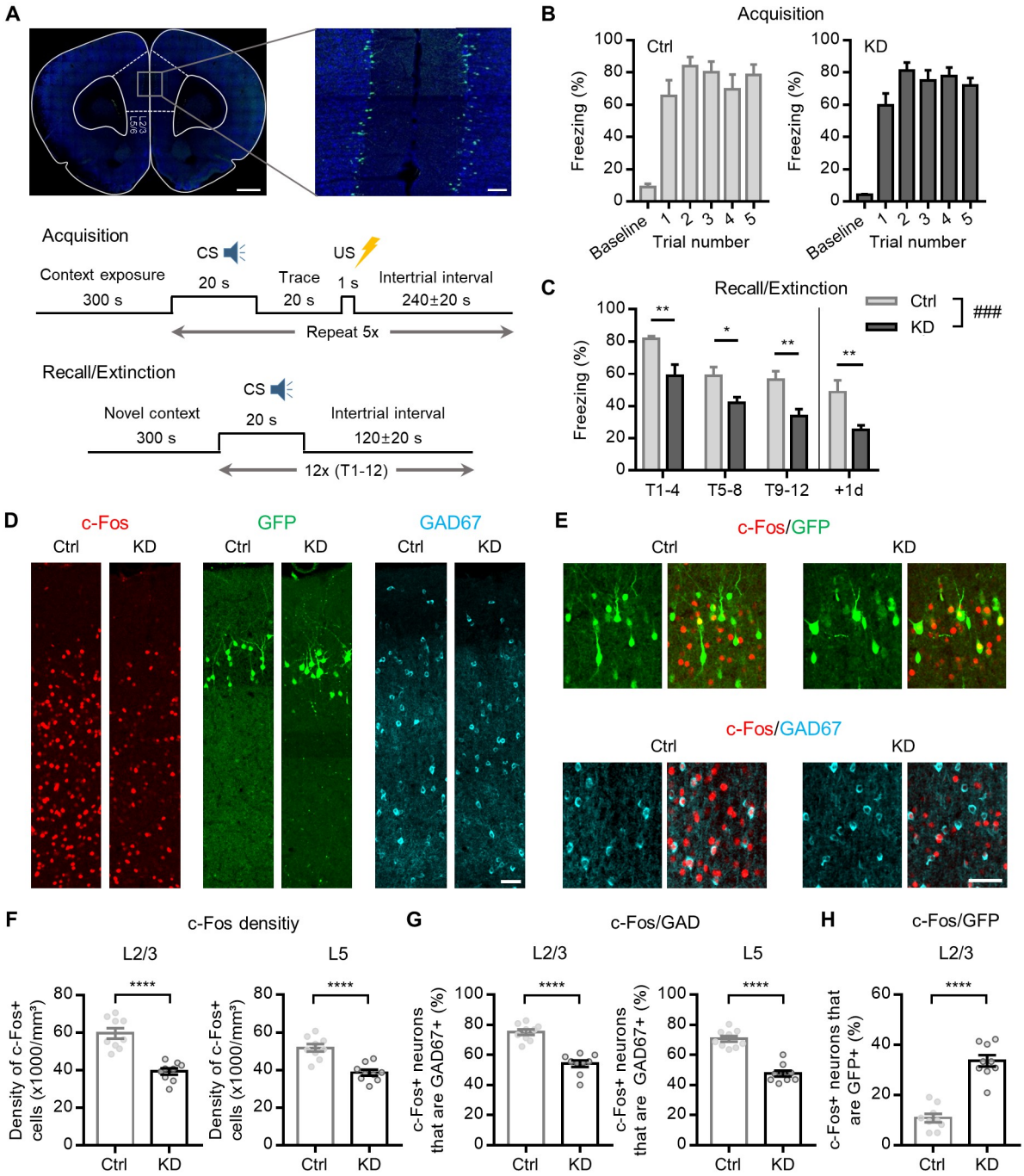

Figure 8. Behavioral effects of Syt7 deficiency in L2/3 PCs of the mPFC

(**A**) *Top*, Representative images showing bilateral expression of U6-GFP in L2/3 of PCs after IUE at E17.5. Scale bar: 1 mm, 100 µm. *Bottom*, Schematic of trace fear conditioning and extinction (tone test) protocol. (**B**) Freezing behavior of control (expressing scrambled shRNA, *Scr*) and Syt7 KD rats during acquisition of tFC. (**C**) Freezing ratio during tone tests on following

122 days. Data are shown as average freezing during T1–T4, T5–T8, or T9–T12 (T, trials). The
123 freezing on T1-T4 was significantly lower in KD rats suggesting that formation of trace memory
124 was impaired in Syt7 KD rats (n = 10, 11 for Ctrl and KD, respectively; P = 0.0007, F(1, 19) =
125 16.43, two-way repeated measures ANOVA; P = 0.0064, 0.0211, 0.0064, 0.0064; Holm-Sidak
126 test). (**D**) Representative images of c-Fos immunoreactivity in the prelimbic cortex of control
127 or Syt7 KD rats 90 min after tFC acquisition. c-Fos (*left*, *red*, Cy5) and GAD67 (*right*, *cyan*, Cy3)
128 were immunostained in the same brain slice expressing U6-GFP (*middle*; *green*). Scale bar, 50
129 µm. (**E**) Exemplar images of c-Fos positive neurons expressing GFP (*top*) or GAD67 (*bottom*)
130 in control (*left*) or Syt7 KD rats (*right*). Scale bar, 50 µm. (**F-H**) Effects of Syt7 KD on c-Fos
131 density (*F*) and percentage of c-Fos positive neurons co-labeled with GAD67 (*G*) or GFP (*H*) in
132 L2/3 or L5 of prelimbic cortex (n = 9, 9 for Ctrl and KD, respectively). *Open symbols*, individual
133 data. All statistical data are represented as mean ± S.E.M.; ****, P＜0.0001; unpaired t-test.
134

135

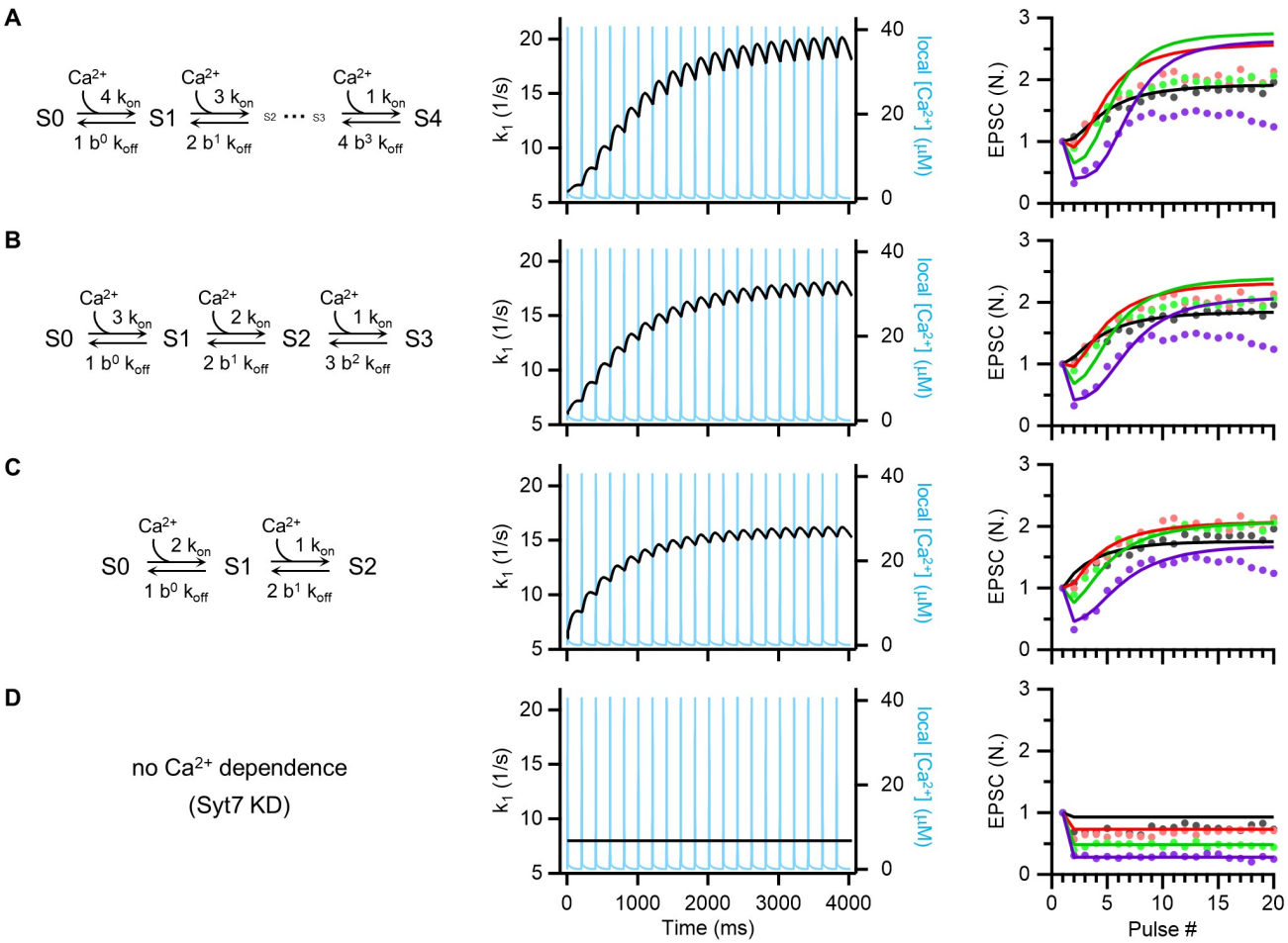

136 **Figure 9. STP model in light of known Ca^{2+} binding kinetics of Syt7**

137 (**A-D**) *Left*, Schematic of allosteric calcium binding to Syt7. The number of Ca^{2+} bound to Syt7
138 was denoted as # in 'S#' in the reaction scheme. k_{on} = 7/μM/s, k_{off} = 10/s. *Middle*, Simulated
139 changes of k_1 (*black*) in response to 5 Hz train of Ca^{2+} transients (*light blue traces*). The priming
140 step of the simple refilling model was assumed to be catalyzed by full Ca^{2+}-bound form of Syt7.
141 Accordingly, Ca^{2+}-dependent increase in k_1 was calculated as $K_{1,max}$ multiplied by a fraction of
142 full Ca^{2+}-bound form of Syt7. We assumed that local $[Ca^{2+}]_i(t)$ follows a Gaussian function: $(1/\sigma$
143 $\sqrt{2\pi})\exp[-(t-t_p)^2/2\sigma^2]$, in which t_p = 0.25 ms and σ = 0.085 ms. *Right*, Fits of the Syt7 model to
144 the STP data. To fit this model to the STP data, $K_{1,max}$ was set to 300/s (*A*), 220/s (*B*), and 180/s
145 (*C*). Cooperativity factor (*b*) was set to 0.35 (*A*), 0.2 (*B*), and 0.05 (*C*). k_1 is set to be constant
146 for Syt7 KD (*D*). Same frequency color codes were used as in ***Figure 1***.

Supplementary Figures

Progressive overfilling of readily releasable pool underlies short-term facilitation at recurrent excitatory synapses in layer 2/3 of the rat prefrontal cortex

Jiwoo Shin[1,2], Seung Yeon Lee[2], Yujin Kim[1,2*], Suk-Ho Lee[1,2*]

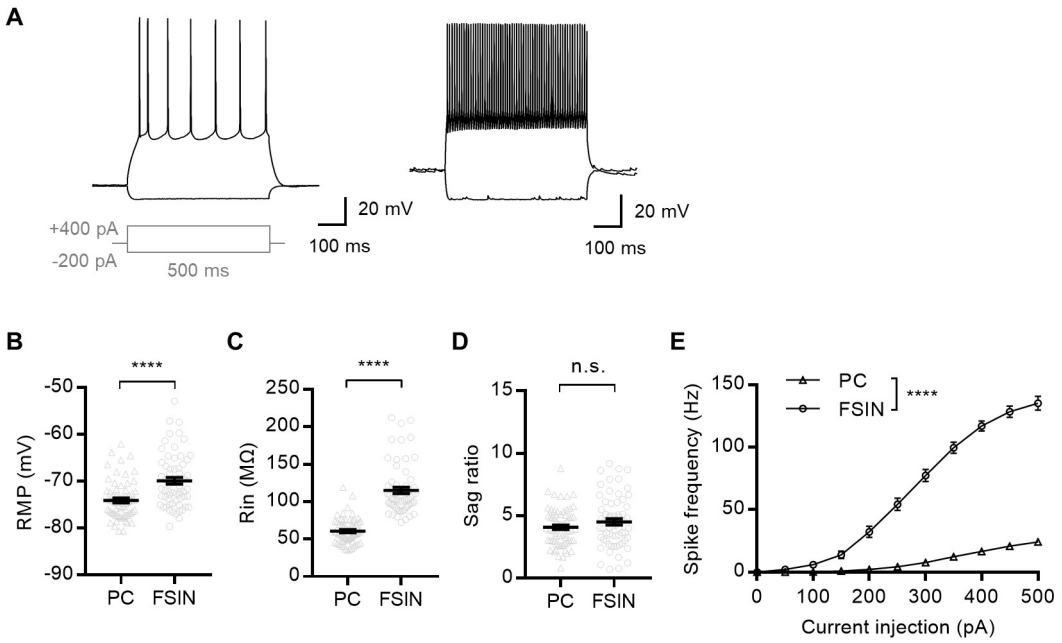

Figure 1—figure supplement 1. Intrinsic membrane properties of mPFC neurons.

(**A**) Neuronal subtypes in mPFC layer 2/3. Cells were characterized based on their electrophysiological properties (n = 66, 64 for PC and FSIN, respectively). Representative voltage responses to current injection (-200 or +400 pA) of pyramidal cells (*left*) and fast-spiking interneurons (*right*). (**B-D**) Mean resting membrane potential (*B*), input resistance (*C*), and Sag ratio (*D*) measured in layer 2/3 PCs and FSINs. *Gray symbols*, individual data. (**E**) Current-spike relationship in each cell type. All statistical data are represented as mean ± S.E.M.; n.s. = not significant; ****, $P < 0.0001$; unpaired t-test or two-way ANOVA.

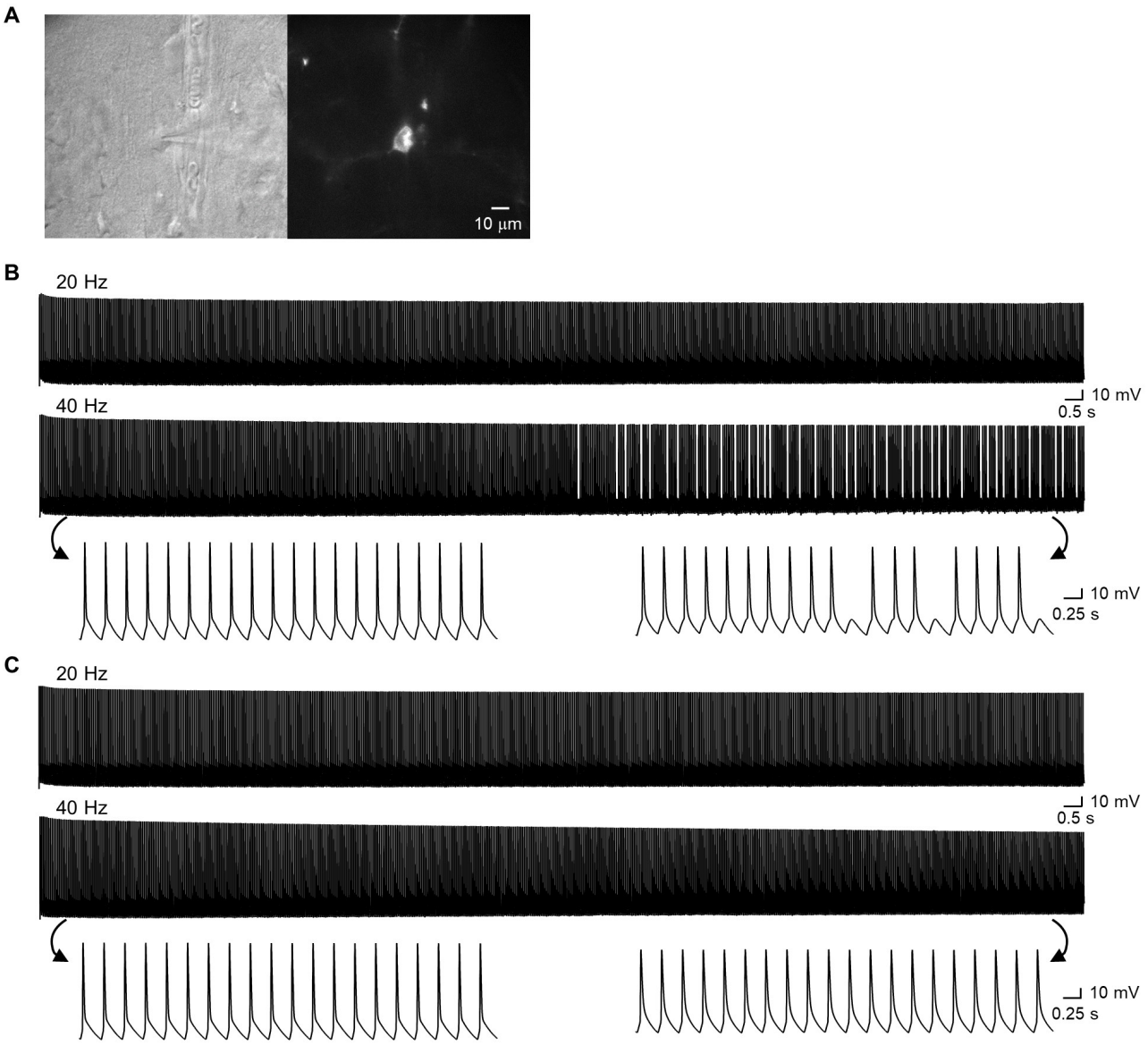

Figure 1—figure supplement 2. Test for consistency of light stimulation in oChIEF-expressing L2/3 pyramidal cells.

(**A**) Representative images of an oChIEF-expressing neuron. Whole-cell recordings were performed from the fluorescently labeled neurons in layer 2/3 of the prelimbic cortex. *Left*, IR-DIC image (60×) of the pyramidal cell under whole-cell patch clamp. *Right*, fluorescence image of td-Tomato in the same cell excited at 530 nm wavelength. (**B**) Current-clamp recordings of action potentials evoked by 600 light pulse trains from an oChIEF-expressing

26 L2/3 cell. For somatic stimulation, we used the typical light stimulation conditions used in STP
27 experiments (5 ms in duration and 4 µm in radius; see *Methods*). Uniform action potentials
28 were produced with high fidelity, albeit not without compromise towards the end of the train
29 in the case of 40 Hz stimulation. Note that these results are similar to previously reported
30 values from neocortical neurons (Lin et al., 2009; Yoon et al., 2020). (**C**) Same experiments as
31 (*B*) but in Syt7 KD pyramidal cells that express oChIEF in L2/3 of the mPFC.
32
33

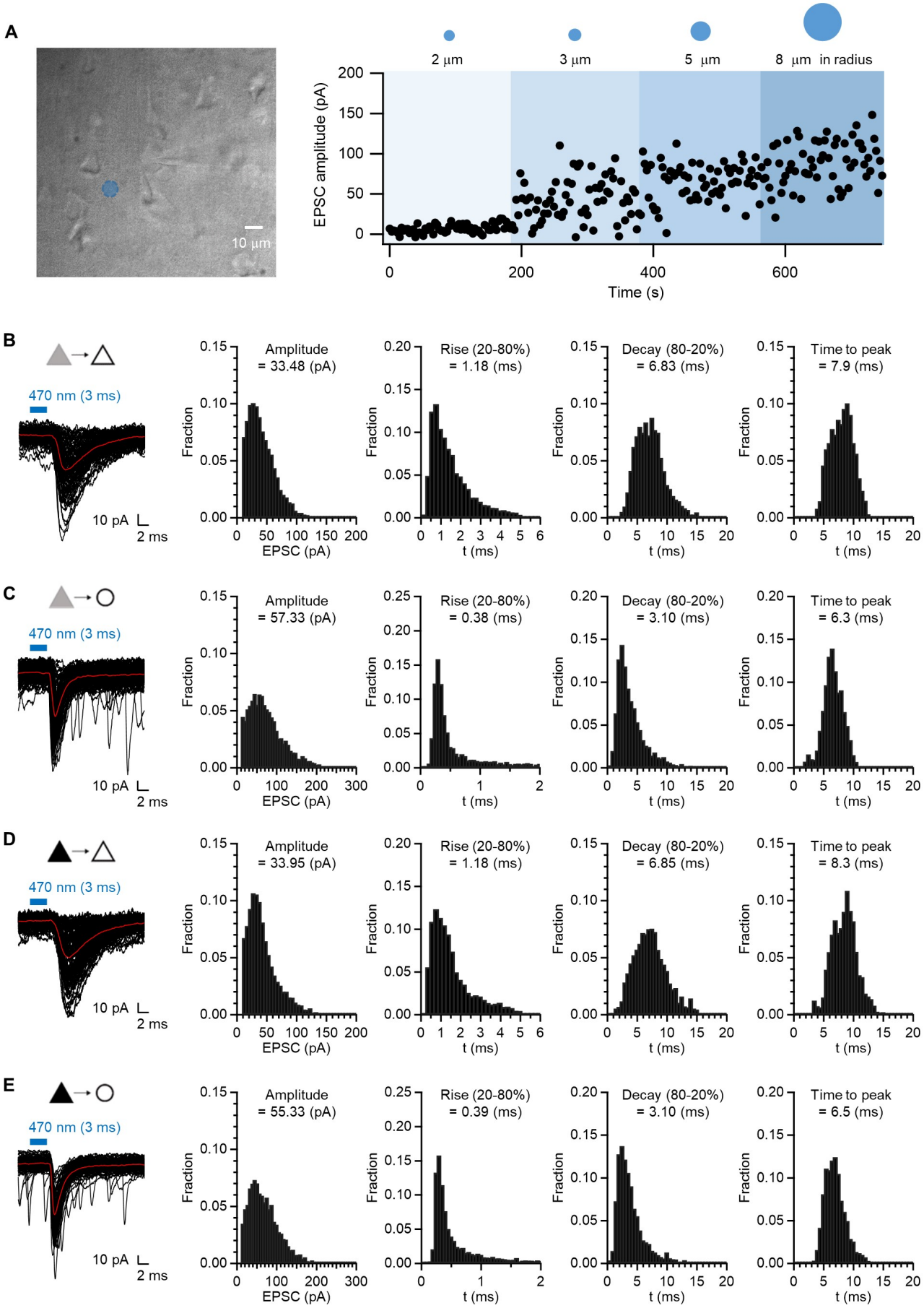
A
10 µm
2 µm
3 µm
5 µm
8 µm in radius
EPSC amplitude (pA)
Time (s)
B
470 nm (3 ms)
10 pA
2 ms
Amplitude = 33.48 (pA)
Rise (20-80%) = 1.18 (ms)
Decay (80-20%) = 6.83 (ms)
Time to peak = 7.9 (ms)
C
Amplitude = 57.33 (pA)
Rise (20-80%) = 0.38 (ms)
Decay (80-20%) = 3.10 (ms)
Time to peak = 6.3 (ms)
D
Amplitude = 33.95 (pA)
Rise (20-80%) = 1.18 (ms)
Decay (80-20%) = 6.85 (ms)
Time to peak = 8.3 (ms)
E
Amplitude = 55.33 (pA)
Rise (20-80%) = 0.39 (ms)
Decay (80-20%) = 3.10 (ms)
Time to peak = 6.5 (ms)
Fraction
EPSC (pA)
t (ms)

35 **Figure 1—figure supplement 3. Properties of EPSCs evoked by minimal stimulation.**

36 (**A**) Optical minimal stimulation. A collimated DMD-coupled LED was used to confine the area
37 of excitation to a small region near the soma. To stimulate a minimal number of excitatory
38 axon fibers, the radius of illumination area was increased from 2 µm by 50% at each step, and
39 selected the smallest illumination area that elicits EPSCs (Yoon et al., 2020) before starting
40 each recording session. The illumination area was in the range of 3 to 8 µm in radius, when
41 measured at the focal plane (typically 3–4 µm) of a 60× water immersion objective (*blue circle*
42 in the photograph). (**B-E**) Properties of minimally stimulated baseline EPSCs (failure-excluded).
43 Medians of frequency distributions are presented. Decay times below 1 ms were excluded
44 from analysis. From left to right, representative traces (100 pulses), EPSC amplitude, rise time
45 (20-80%), decay time (80-20%), and time to peak (from stimulus onset) from WT PC-PC (*B*, n
46 = 81), WT PC-FSIN (*C*, n = 77), Syt7 KD PC-PC (*D*, n = 72), and Syt7 KD PC-FSIN (*E*, n = 78)
47 synapses.
48
49

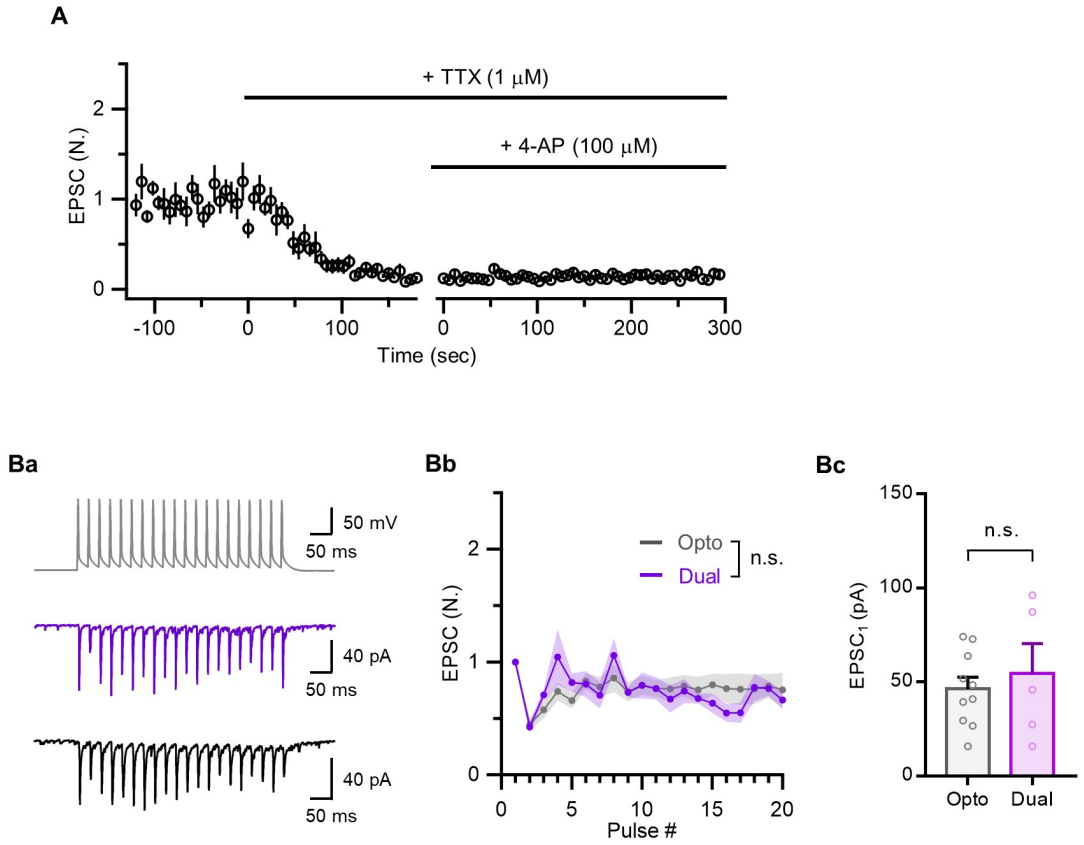

Figure 1—figure supplement 4. Validation of STP of optically evoked EPSCs

(**A**) The high p_v at PC-PC synapses may result from direct photo-stimulation of axon boutons. To test if optically evoked EPSCs depend on APs, the effect of 1 µM tetrodotoxin (TTX) was tested. Applying 1 µM tetrodotoxin (TTX) and additionally 0.1 mM 4-aminopyridine, a D-type K channel blocker abolished optically evoked EPSCs (n = 8). Even when repolarization was hindered by subsequent addition of 100 µM 4-aminopyridine (4-AP), a potassium channel blocker, EPSCs were not rescued. These findings suggest that the light-evoked responses are dependent on APs of presynaptic axon fibers rather than photo-induced depolarization of presynaptic boutons (Little and Carter, 2013). (**B**) Comparison of STP evoked by optical stimulation with that by dual patch techniques. To test validity of STP of photostimulation-evoked EPSCs, we compared STP of unitary EPSCs evoked by dual whole-cell patch at PC-FSIN synapses. Both of EPSC1 and STP at 40 Hz recorded by using paired whole-cell recordings were not significantly different from those evoked by photo-stimulation, supporting the validity of

our optogenetic methods. (**Ba**) Representative EPSC traces evoked by 20-pulse 40 Hz trains stimulation at pyramidal cell to fast spiking interneuron (PC-FSIN) synapses. A train of APs in a presynaptic PC (*top*), evoked EPSCs in a FSIN by dual whole-cell patch clamp (*middle*) or by optical stimulation (*bottom*) under same conditions. (**Bb**) Mean values for baseline-normalized amplitudes of EPSCs evoked by 40 Hz train at PC-FSIN synapses. *Opto*, optical stimulation (n = 10); *Dual*, dual patch techniques (n = 5). STP evoked by the two techniques were not significantly different (two-way repeated measures ANOVA, $F(1, 13) < 0.01$, $P = 0.955$). (**Bc**) Mean values for the first EPSC in different stimulation methods ($P = 0.5724$, unpaired t-test). *Open circles*, individual data. All statistical data are represented as mean ± S.E.M.

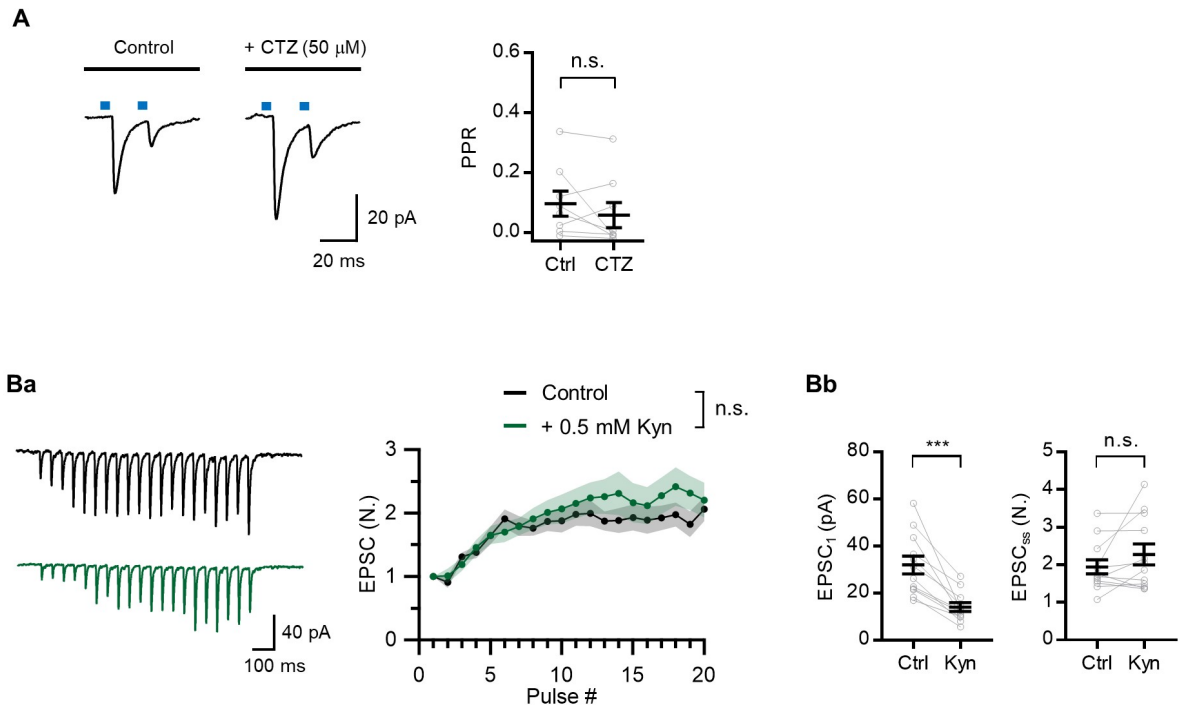

Figure 1—figure supplement 5. Test for AMPAR desensitization and saturation

(**A**) Representative traces of EPSCs evoked by paired-pulse photostmulation at 20 ms ISI (*left*) and mean values for paired pulse ratio (PPR, *right*) before and after applying 50 μM cyclothiazide (CTZ, n = 8), an AMPA receptor (AMPAR) desensitization inhibitor. CTZ induced no significant change in PPR arguing against the possibility that strong PPD is caused by AMPAR desensitization. *Gray symbols*, individual data. (**B**) It has been shown that multi-vesicular release occurs at recurrent excitatory synapses in neocortical L2/3 (Holler et al., 2021). Whereas a single vesicle release is insufficient to saturate postsynaptic AMPARs, an increase in the number of vesicular release during facilitation may saturate AMPAR resulting in underestimation of facilitation. To test this possibility, facilitation at 20 Hz was measured in the presence of 0.5 mM kynurenic acid (Kyn), a fast competitive antagonist (Diamond and Jahr, 1997; Wadiche and Jahr, 2001). Fast blockade of AMPA receptors did not have significant effects on short-term facilitation at excitatory synapses in the mPFC L2/3, suggesting that AMPAR saturation may not be significant during facilitation. (**Ba**) Representative EPSC traces (*left*) and average of baseline-normalized EPSCs (*right*) evoked by 40 Hz 20-pulse trains in

control and in the presence of 0.5 mM kynurenic acid (Kyn). Although facilitation was slightly increased by Kyn, it was not statistically significant (n = 12; two-way repeated measures ANOVA, F (1, 22) = 0.575, P = 0.456). The slightly higher facilitation may result from reduced blocking efficiency of Kyn upon increased glutamate concentration in the synaptic cleft (Tong and Jahr, 1994; Meyer et al., 2001). (**Bb**) Mean values for the baseline EPSC (*left*) and the steady-state EPSC (*right*) before and after applying 0.5 mM kynurenate as shown in *Ba*. The baseline EPSC was reduced by Kyn to 43.5% of control. *Gray symbols*, individual data. All statistical data are represented as mean ± S.E.M.; n.s. = not significant; ***, $P < 0.001$; paired t-test.

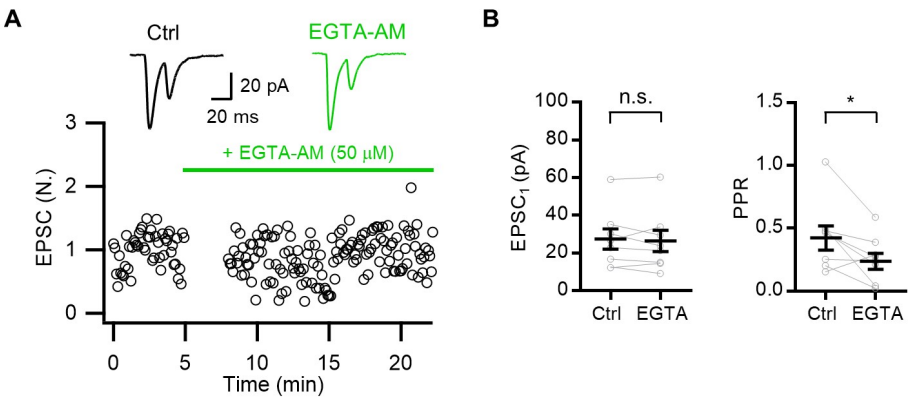

101 **Figure 2—figure supplement 1. Effects of EGTA-AM on synaptic transmission**

102 (**A**) Representative traces (*top*) and time courses of normalized amplitudes of the first EPSCs
103 (*bottom*) during paired-pulse photostimulation at 20 ms ISI in control and in the presence of
104 50 μM EGTA-AM (n = 8). The green horizontal bar indicates application of 50 μM EGTA-AM.
105 (**B**) Mean values for the first EPSC (*left*) and PPR (*right*) before and after EGTA-AM application.
106 *Gray symbols*, individual data. All statistical data are represented as mean ± S.E.M.; n.s. = not
107 significant; *, $P < 0.05$; paired t-test.

108

109

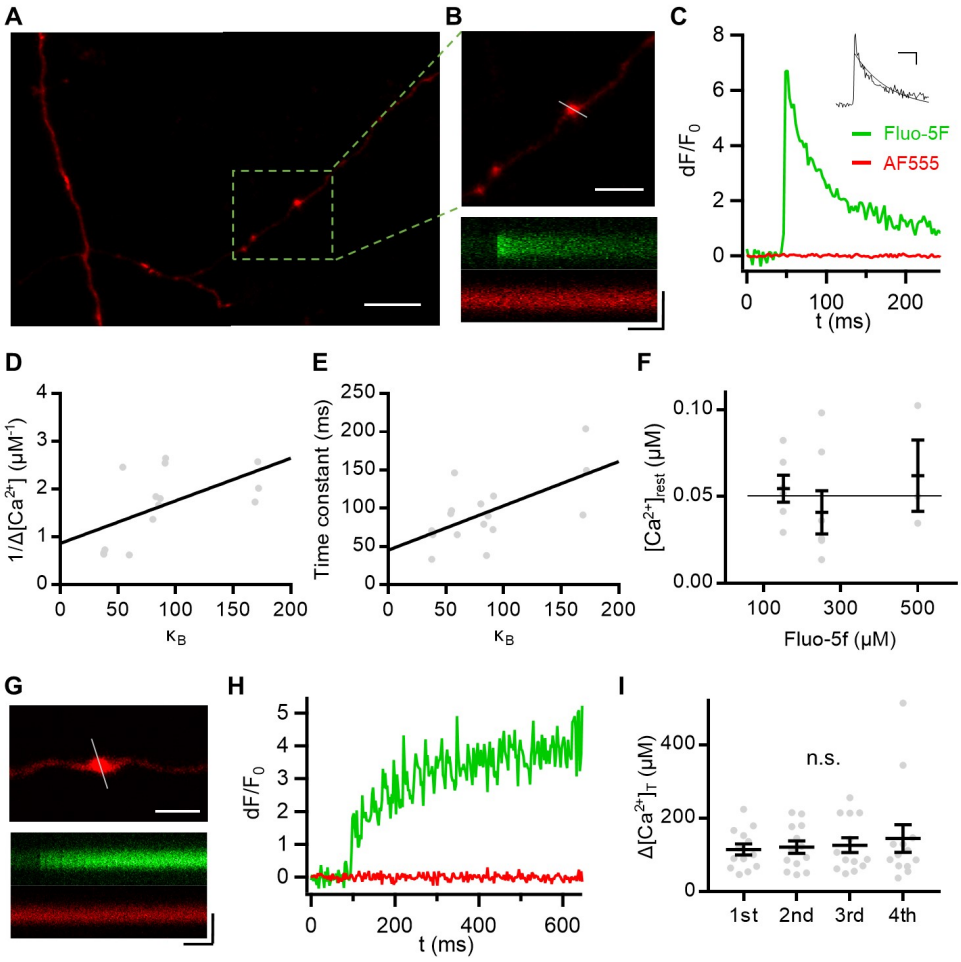

110 **Figure 2—figure supplement 2. Presynaptic calcium kinetics at boutons of layer 2/3**
111 **pyramidal cells**

112 (**A-C**) A mixture of Fluo-5F (150, 250 or 500 μM) and Alexa Flour 555 was loaded on their
113 axonal boutons of L2/3-PCs through whole-cell patch techniques for dual excitation
114 ratiometric measurements of the cytosolic [Ca^{2+}] at axonal boutons. (**A**) The long-branched
115 stretch of axon from L2/3 PCs visualized through maximum fluorescence intensity projection
116 using confocal laser scanning of AF555 perfused via a patch clamp pipette. Scale bar, 10 μm.
117 (**B**) *Top*, the selected bouton for recordings, among the three, is displayed with the
118 corresponding scanning line. Scale bar, 5 μm. *Bottom*, Line-scan images for fluorescence of
119 Fluo-5F and AF555. Scale bars, 50 ms and 2 μm. (**C**) Baseline-normalized fluorescence changes
120 evoked by an AP. Fluorescence intensities were spatially averaged over the bouton shown in

121 (*B*), background-subtracted and normalized to the baseline value (dF/F_0). *Inset*, Ca^{2+} transient
122 estimated from dF/F_0. Scale bar, 50 ms and 100 nM. (**D, E**) The kinetic parameters of an AP-
123 CaT were determined from a plot for the inverse of AP-evoked [Ca^{2+}] increment ($1/\Delta[Ca^{2+}]$) *vs*.
124 calcium binding ratio (κ_B; Eq. 4 in *Material and Methods*). (**D**) Reciprocal plot of the AP-induced
125 [Ca^{2+}] changes ($1/\Delta[Ca^{2+}]$) vs. corresponding calcium binding constants (κ_B) according to Eq. 2
126 (n = 14). A linear fit to the plot gave the amplitude of AP-CaT (A_{Ca} = 1.16 μM) from the y-
127 intercept, representing the amplitude of free [Ca^{2+}] increase in the absence exogenous Ca^{2+}
128 buffer. The calcium binding ratio of endogenous static Ca^{2+} buffers (κ_S) was estimated as 96
129 from the x-intercept of the linear regression based on Eq. 2 in *Material and Methods*. Linear
130 regression line, P = 0.035. (**E**) Plot of [Ca^{2+}] decay time constant versus κ_B (n = 16). The time
131 constant for [Ca^{2+}] decay from mono-exponential fit was plotted vs. κ_B, and a linear regression
132 based on Eq. 3 yielded the κ_S value of 77 from the x-intercept. The y-intercept was 43 ms, an
133 estimate for a dye-independent value for Ca^{2+} decay time constant (τ_c) (Eq. 3 in *Material and*
134 *Methods*). Linear regression line, P = 0.011. (**F**) Resting [Ca^{2+}] measured from basal
135 fluorescence ratio using Eq. 1 in *Material and Methods* as a function of [Fluo-5F] in patch
136 pipettes. The horizontal line indicates 50 nM. The mean $[Ca^{2+}]_{rest}$ at three different
137 concentrations of Ca^{2+} indicator dye were not different and measured as 50 nM, suggesting
138 that the dye did not influence $[Ca^{2+}]_{rest}$. (**G-I**) Strong PPD and the subsequent STF may be
139 caused by Ca^{2+} channel inactivation and Ca^{2+}-dependent facilitation (CDF) of calcium influx
140 into presynaptic boutons, respectively. To test these possibilities, we measured presynaptic
141 Ca^{2+} increments evoked by each of successive APs applied in a train at 40 Hz. (**G**) Fluorescence
142 signals from a selected bouton with a scanning line. *Scale bars*, 3 μm (*top*), 100 ms and 2 μm
143 (*bottom*). (**H**) Normalized fluorescence (dF/F_0) responses to a train of APs at 40 Hz. (**I**) Total
144 Ca^{2+} increments ($\Delta[Ca^{2+}]_T$; free plus bound form) are plotted against the number of APs in the
145 train (n = 13). $\Delta[Ca^{2+}]_T$ were calculated based on Eq. 2 with κ_S set to 90. No significant change
146 was observed for the estimates of $\Delta[Ca^{2+}]_T$ at each of first 4 APs during 40 Hz train, indicating
147 that contributions of Ca^{2+} channel inactivation and CDF to STP are unlikely. Mean ± S.E.M.,
148 One-way ANOVA; n.s. = not significant.

149

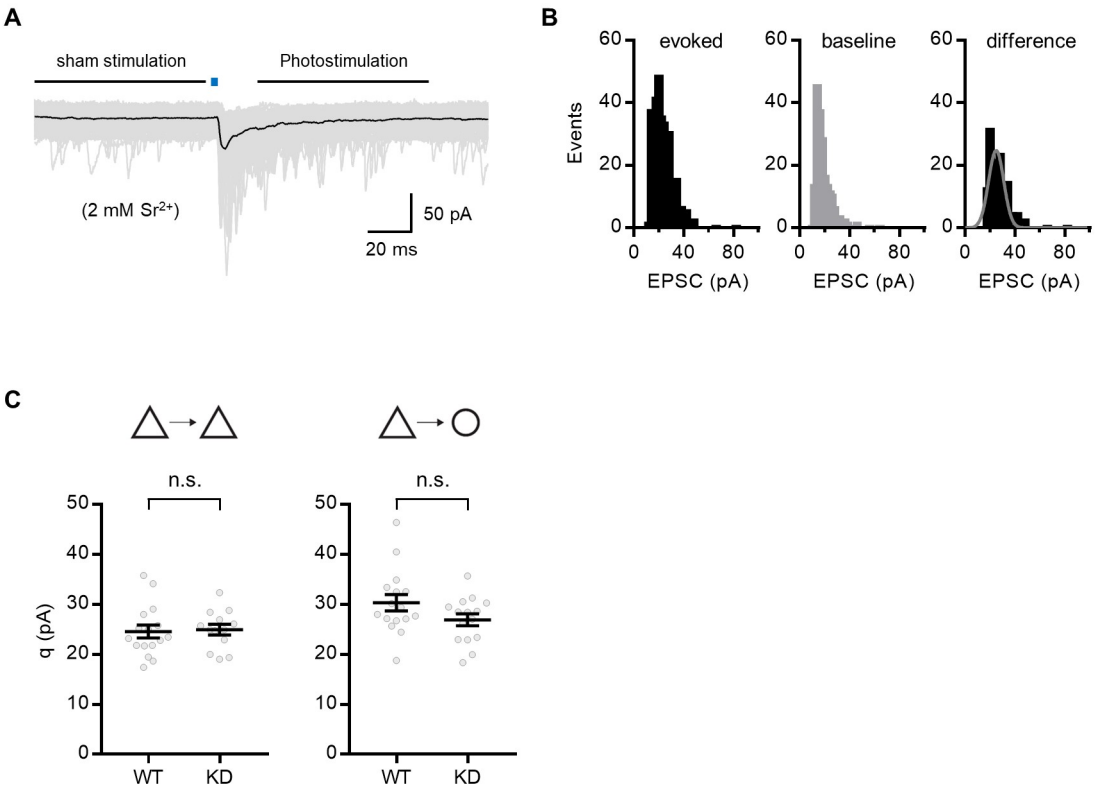

150 **Figure 3—figure supplement 1. Quantal size estimated from Sr^{2+}-induced asynchronous**
151 **release.**

152 (**A**) Representative traces (100 pulses) from PC-PC synapses. Black bars indicate the detection
153 window (100 ms) for release events in sham stimulation (*left bar*) and photostimulation (*right*
154 *bar*). (**B**) Representative distribution of asynchronous EPSCs at PC-PC synapses. *Left*, after
155 photostimulation. *Middle*, before stimulation. *Right*, difference between left and middle
156 panels. The difference distribution was fitted with a Gaussian function (m = 24.93, σ = 6.09).
157 (**C**) Comparisons of estimates for quantal size (q) between WT and Syt7 KD synapses. From
158 left to right: PC-PC (n = 16, 13 for WT and KD, respectively), PC-FSIN (n = 16, 15). *Gray symbols*,
159 individual data. All data are represented as mean ± S.E.M., unpaired t-test; n.s. = not
160 significant.
161

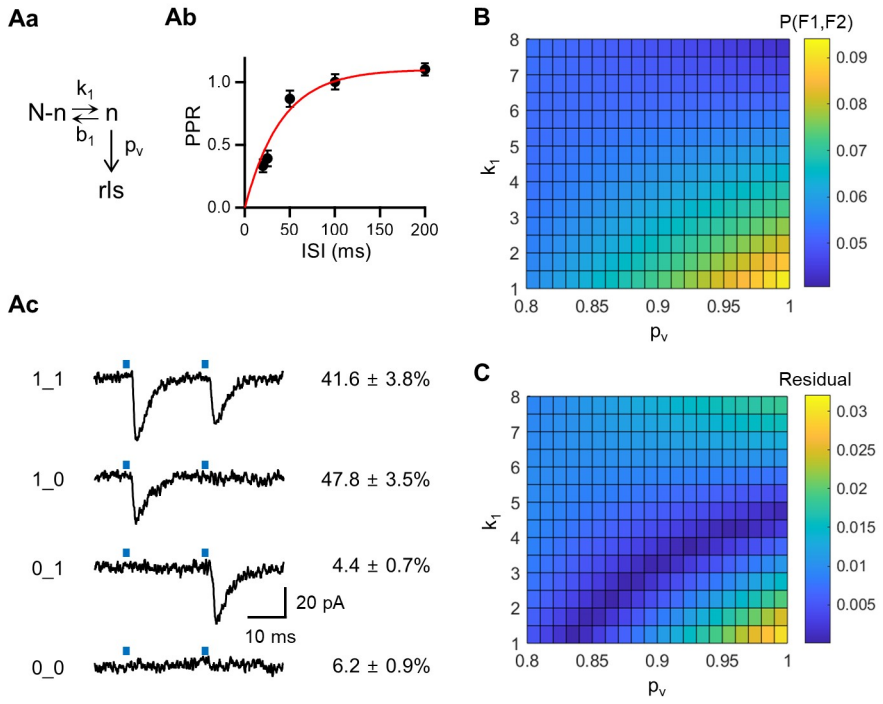

Figure 3—figure supplement 2. Analysis of double failure rate supports high p_v at excitatory synapses

(**Aa**) Schematic of simple refilling model. (**Ab**) An exponential fit to the PPR plot as a function of ISIs reproduced from *Figure 1G*. *Fitted function*, PPR = 1.1 [1 − exp(− t/43.5 ms)]. (**Ac**) Representative traces for four combinations of success and failure of 1st and 2nd EPSCs evoked by paired pulses with ISI of 20 ms at PC-PC synapses, showing successes in both pulses (1_1), failures in both pulses (0_0), and mixed responses (1_0; 0_1). On the right side of each trace, corresponding observation probability is shown in percentages (mean ± S.E.M. n = 57). (**B-C**) Plots of the calculated P(F1, F2) values (*B*) and their differences (*C*) from the observed value (6.2%) under the simple refilling model are displayed on the plane of k_1 versus p_v.

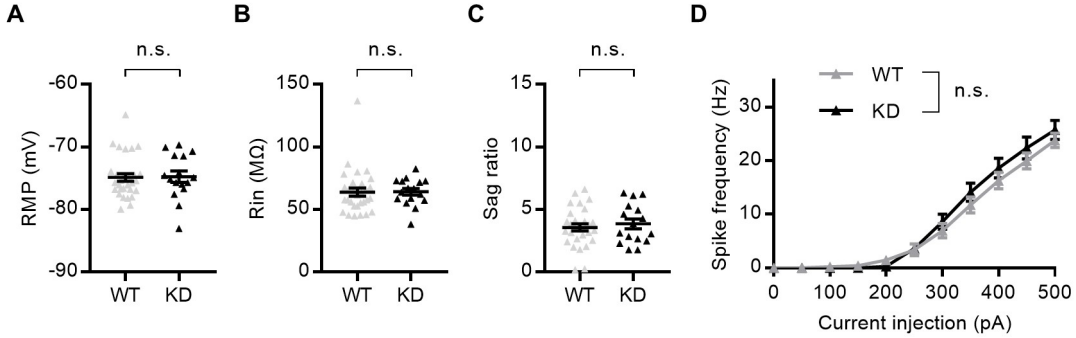

174 **Figure 5—figure supplement 1. Little effects of Syt7 KD on intrinsic properties of neurons**

175 Whole-cell recordings were performed from the fluorescently labeled pyramidal neurons in
176 the prelimbic L2/3 of WT (n = 30) or Syt7 KD (n = 16) rats. (**A**) Resting membrane potential. (**B**)
177 Input resistance. (**C**) Sag ratio. *Filled triangles*, individual data. (**D**) Current-spike frequency
178 relationship in WT and KD cells. All statistical data are represented as mean ± S.E.M., unpaired
179 t-test or two-way ANOVA; n.s. = not significant.

180

181

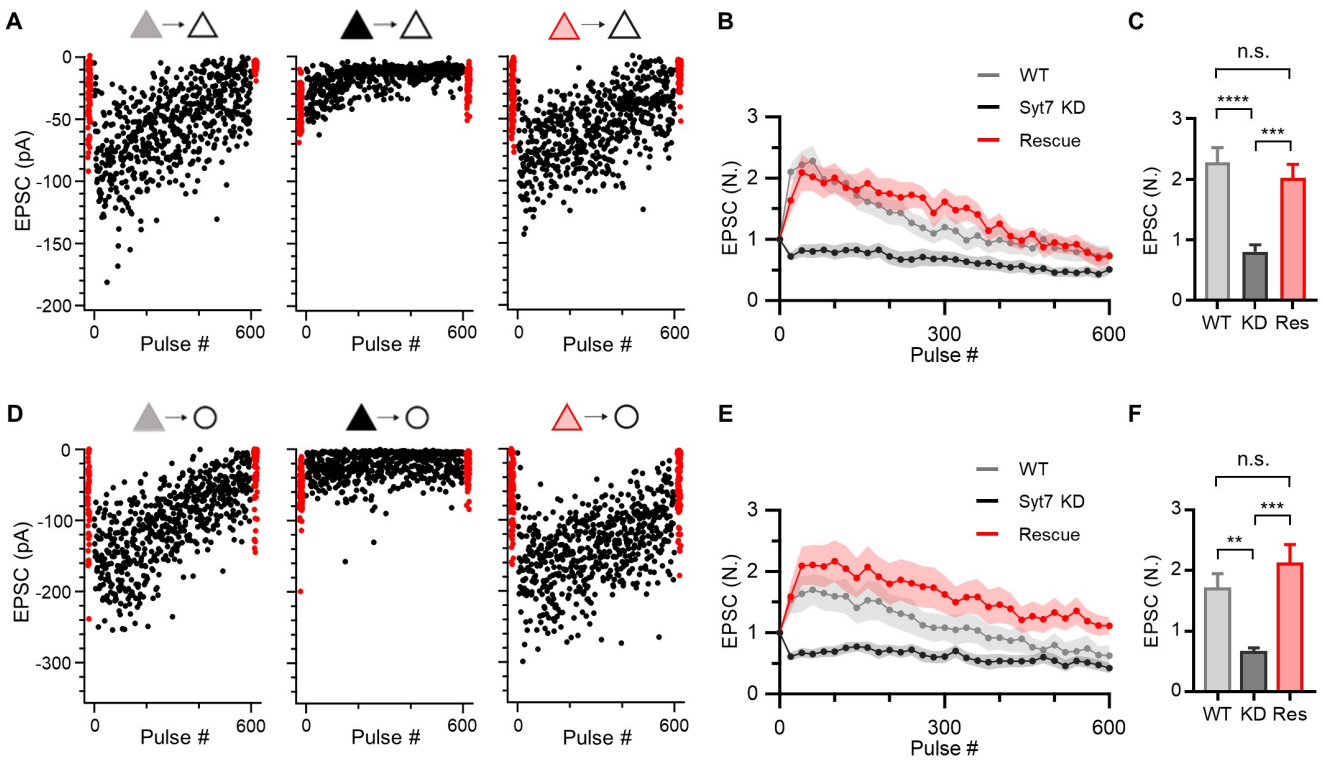

182 **Figure 5—figure supplement 2. Presynaptic expression of Syt7 rescues facilitation at L2/3**
183 **excitatory synapses**

184 (**A, D**) Representative amplitudes of EPSC trains evoked by 600-pulse 10 Hz trains (flanked by
185 2 baseline periods comprised of 40 pulses each) at PC-PC (*A*) and PC-FSIN (*D*) synapses, in
186 which presynaptic WT (*left, gray triangles*) pyramidal cells and those transfected with plasmid
187 encoding shRNA against Syt7 (sh-Syt7, KD, *middle, black triangles*) or sh-Syt7 plus Syt7
188 insensitive to shRNA (rescue, *right, red triangles*). (**B, E**) STP of EPSCs evoked by 600-pulse
189 trains at 10 Hz at L2/3 PC-PC (*B*; n = 9, 10, 7; WT, Syt7 KD, Rescue, respectively) and PC-FSIN
190 (*E*; n = 12, 10, 8) synapses. Each data point represents an average from a moving window of
191 20 pulses, normalized to the baseline EPSC. (**C, F**) Mean values of 41-60th pulses from *B* and *E*.
192 Mean ± S.E.M.; n.s. = not significant; **, $P < 0.01$; ***, $P < 0.001$; ****, $P < 0.0001$; one-way
193 ANOVA with Tukey's post-hoc test.

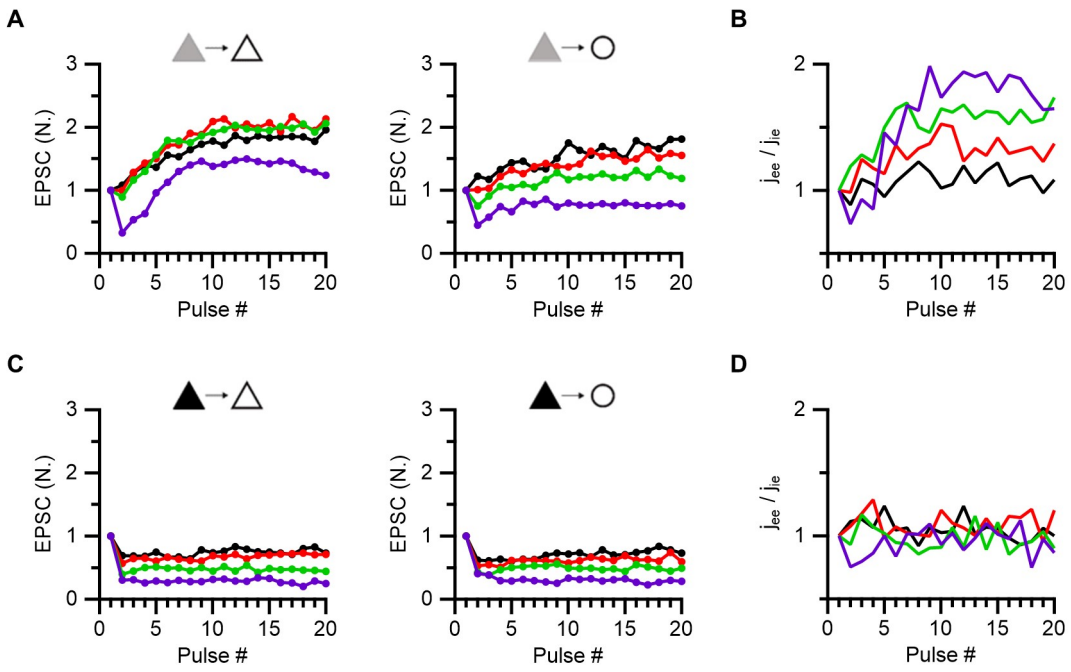

194 **Figure 8—figure supplement 1. Activity-dependent increase in the synaptic weight ratio at**

195 **PC-PC to at PC-FSIN connections (J_{ee}/J_{ie}) is abolished by Syt7 KD**

196 (**A, C**) Average amplitudes of baseline-normalized EPSCs during 20-pulse trains at frequencies
197 from 5 to 40 Hz at PC-PC (*left*) and PC-FSIN (*right*) synapses in WT (*A*) and Syt7 KD (*C*). Data
198 are reproduced from ***Figure 1*** (*A*) and ***Figure 5*** (*C*). (**B, D**) Relative synaptic weights of
199 excitatory input to PCs over that onto FSINs (*Jee/Jie*) in WT (*B*) and Syt7 KD (*D*). Note that
200 excitatory influence (*Jee/Jie*) to the recurrent network increases as the firing number and
201 frequency increase in WT but not in Syt7 KD.

202

203

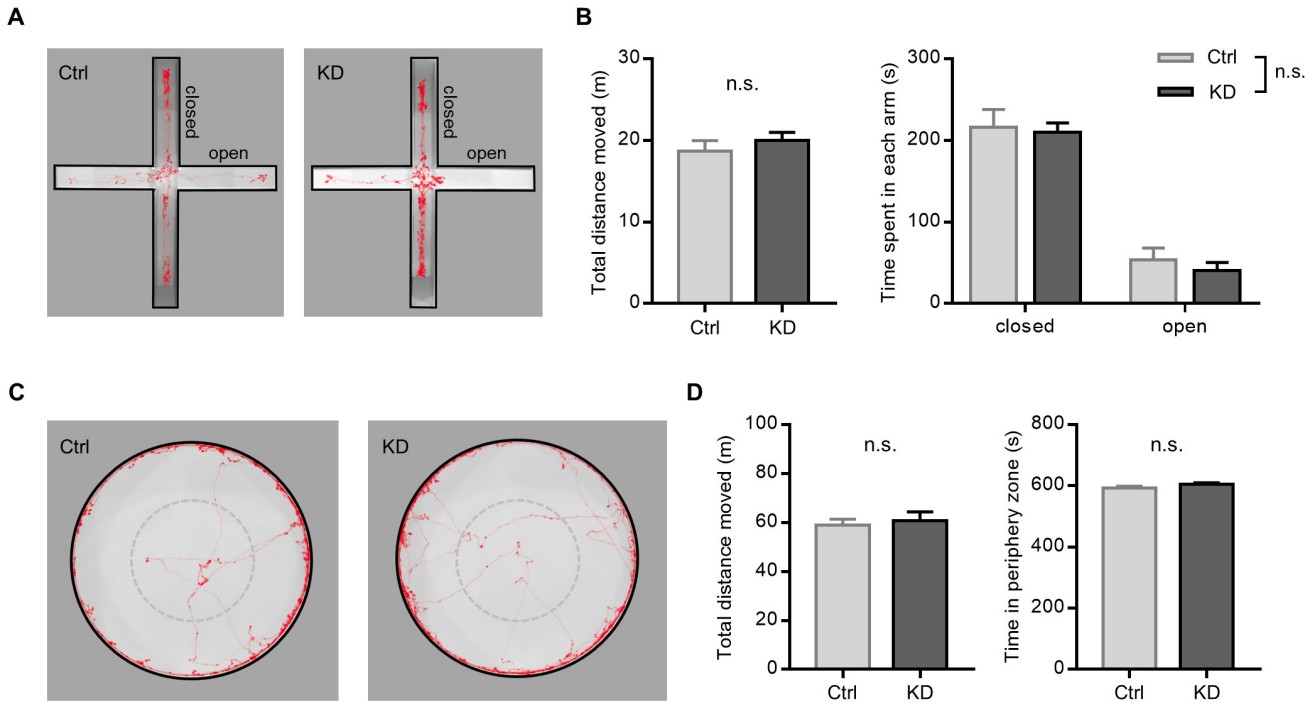

Figure 8—figure supplement 2. Locomotor activity and anxiety levels in Syt7 KD rats using OFT and EPM

(**A, C**) Representative tracking trace of the elevated plus maze (*A*) and open field test (*C*). (**B, D**) Mean values for total distance moved (*left*) and time spent (*right*) in each arm (*B*) or in periphery zone (*D*) in control (n = 13) or Syt7 KD rats (n = 9). Mean ± S.E.M.; Unpaired t-test or two-way ANOVA; n.s. = not significant.

212 ## References

213 Diamond JS, Jahr CE (1997) Transporters buffer synaptically released glutamate on a
214 submillisecond time scale. J Neurosci 17:4672-4687.
215 Holler S, Kostinger G, Martin KAC, Schuhknecht GFP, Stratford KJ (2021) Structure and
216 function of a neocortical synapse. Nature 591:111-116.
217 Lin JY, Lin MZ, Steinbach P, Tsien RY (2009) Characterization of engineered channelrhodopsin
218 variants with improved properties and kinetics. Biophys J 96:1803-1814.
219 Little JP, Carter AG (2013) Synaptic mechanisms underlying strong reciprocal connectivity
220 between the medial prefrontal cortex and basolateral amygdala. J Neurosci 33:15333-
221 15342.
222 Meyer AC, Neher E, Schneggenburger R (2001) Estimation of quantal size and number of
223 functional active zones at the calyx of Held synapse by nonstationary EPSC variance
224 analysis. J Neurosci 21:7889-7900.
225 Tong G, Jahr CE (1994) Multivesicular release from excitatory synapses of cultured
226 hippocampal neurons. Neuron 12:51-59.
227 Wadiche JI, Jahr CE (2001) Multivesicular release at climbing fiber-Purkinje cell synapses.
228 Neuron 32:301-313.
229 Yoon JY, Lee HR, Ho WK, Lee SH (2020) Disparities in Short-Term Depression Among Prefrontal
230 Cortex Synapses Sustain Persistent Activity in a Balanced Network. Cereb Cortex
231 30:113-134.

232